*Electronic Research Archive*

https://www.aimspress.com/journal/era

ERA, 33(5): 2762–2799.
DOI: 10.3934/era.2025122
Received: 01 March 2025
Revised: 06 April 2025
Accepted: 21 April 2025
Published: 09 May 2025

*Research article*

# Chaotic behavior of a new fractional-order financial system and its predefined-time sliding mode control based on the RBF neural network

**Shanshan Yang and Ning Li***

College of Sciences, Northeastern University, Shenyang 110819, China

* **Correspondence:** Email: lining80@163.com.

**Abstract:** Fractional-order financial systems hold significant importance in practical situations. In this work, a novel fractional-order financial system considering the non-constant elasticity of demand was presented, and the system's complex dynamics were studied. The results demonstrated that the system can exhibit diverse chaotic dynamics and periodic oscillations, which are influenced by different fractional orders and system parameters. Then, to stabilize the proposed chaotic system with uncertainties and achieve predefined-time synchronization of master-slave systems, an effective sliding mode control strategy utilizing the RBF neural network was put forward. In real financial markets, uncertainties and perturbations occur suddenly, and excessive control input can lead to resource inefficiency. Therefore, unlike other papers that rely on conservative estimations using upper bounds, this paper used RBF neural network approximation to design a more flexible and robust controller while reducing the control input. Simulation findings reveal that this approach requires less control input than traditional methods without the RBF neural network and converges more rapidly than finite-time, fixed-time, and other predefined-time sliding mode control strategies with the RBF neural network, which validates the feasibility of this approach. Finally, the proposed chaotic system and control method were successfully applied to secure encryption, demonstrating their practical value.

**Keywords:** fractional-order financial system; sliding mode control; predefined-time synchronization; RBF neural network; secure encryption

## 1. Introduction

Fractional calculus, or non-integer calculus, has existed for more than 300 years [1]. Compared to integer-order derivatives, fractional derivatives have memory effect [2], meaning the fractional-order (FO) models rely on both the present and prior states. Riemann-Liouville (RL) and Caputo fractional derivatives serve to describe complex and nonlinear phenomena that integer-order derivatives fail to capture accurately. In other words, FO systems are more suitable for practical applications. At present,

fractional calculus has been widely employed in multiple research fields, including control theory [3], biomedicine [4], finance [5], and other fields [6].

Chaos theory concentrates on the analysis of nonlinear models that are particularly susceptible to slight disturbances in the initial stage [7]. Since the pioneering work pointed out the possibility of chaotic dynamics in economic models [8], bifurcation and control problems in chaotic financial systems have been comprehensively studied and implemented. Ma and Chen [9] analyzed the bifurcation phenomenon and the general properties of the nonlinear financial model when $c - b - abc \leq 0$. In a subsequent work [10], they studied the case when $c - b - abc \geq 0$. In 2009, Gao and Ma [11] put forward a delayed-time financial chaos system and explored its qualitative features like Hopf bifurcation. Tacha et al. [12] suggested a fresh chaotic model and gave its circuit simulation. The $x^2$ term of the second differential equation has been replaced with $x^4$ [13], and it was further transformed into a higher-order term $x^2 + x^4$ [14]. Because the elasticity of market demand is affected by many factors in real life, a financial system with non-constant elasticity of demand was put forward [15]. In 2021, Subartini et al. [16] studied a novel finance system and discovered symmetry, equilibrium points, as well as multistability of the model. Based on financial principles, Wei et al. [17] suggested a new financial risk contagion dynamic model. Yan et al. [18] proposed a new method for modeling the chaotic dynamics of financial data, and the money market case was simulated. In 2025, Johansyah et al. [19] introduced the nonlinear term of the absolute value function to establish a new chaotic system, and analyzed the enhanced chaotic behavior of the new model from many aspects. Considering the gross domestic product (GDP) growth rate, unemployment rate, and vacancy availability rate, a new 6D model with three time lags was established [20]. These papers constructed new systems by altering nonlinear terms or incorporating additional economic variables. Variables in finance, including the GDP, production data, and stock prices, can exhibit enduring memories, meaning that past economic activity influences current and future trends. Therefore, research on fractional financial systems has become increasingly extensive. Xu et al. [21] considered the delay to be the bifurcation parameter and gave a sufficient condition for Hopf bifurcation to occur in an innovative FO model. Yao et al. [22] explored the dynamic behavior of the FO Rocard model. Cui and Liu [23] used mathematical models to computationally model the financial system. In 2023, Li et al. [24] established an advanced 4D FO financial model and analyzed its finite-time synchronization. In 2024, Diabi et al. [25] studied bifurcation, chaos, and control of FO discrete financial systems. Xu et al. [26] constructed an FO financial risk system (FFRS), studied its dynamic behavior and function projection synchronization, and interpreted the dynamic results. However, in real financial markets, the elasticity of demand is not constant, and many of the above studies only studied the case of constant demand elasticity. Based on this consideration, we developed a new chaotic system, and then extended it to an FO system, which is more consistent with the real financial market and describes more complex financial behaviors.

Since Pecora and Carroll [27] proved the implementability of synchronizing chaotic models, it has become a key focus in chaos control research. In financial markets, small initial disturbances can lead to large fluctuations. This nonlinear behavior is often more prominent in systems with uncertain and perturbed terms. Controlling the synchronization of chaotic models helps to better understand and predict the nonlinear response of the market. There are many chaos control methods, such as sliding mode control (SMC) [28], adaptive control [29], and linear control [30]. The SMC method focuses on constructing the sliding surface and controller, guiding this system state along the predetermined "sliding mode" trajectory, making it a reliable and robust control method. Wang et al. [31] explored the finite-

time terminal SMC of a four-dimensional FO financial chaotic system with a neural network. A new control law was established and an adaptive integral SMC was used to realize synchronization [32]. The authors focused more on FO financial chaotic systems and adaptive finite-time SMC [33]. In chaos control, the study of stability time, in addition to control methods, is also a crucial part. A shorter stability time leads to faster synchronization. Stability time can be divided into different types, with asymptotic-time control being the first method [34], capable of maintaining the system's stability. However, its convergence rate is slow and its precision is constrained. Subsequently, finite-time control was proposed [35], which has a faster convergence speed but is sensitive to the starting values. This shortcoming was addressed by fixed-time control [36]. However, the creation of a fixed-time controller is complex. To address the aforementioned issue, pioneering predefined-time synchronization techniques have gained attention. It allows users to set the system's convergence time according to their specific requirements, offering high flexibility and predictability. A Lyapunov function that depends only on the user-specified time was designed [37]. A new Lyapunov function in polynomial form was introduced [38], which facilitates controller design. In 2022, a function with an additional term was designed [39]. Xue and Liu [40] changed the exponential. Previous research proved that predefined-time control can simplify theoretical analysis and calculation. Therefore, exploring and applying sliding mode control techniques by combining the strengths of SMC and predefined-time control is a worthwhile topic of study. An innovative sliding surface was presented to guarantee the convergence of synchronization errors within a specified time [41]. A time-synchronized predefined-time SMC was implemented in [42]. Furthermore, Jia et al. [43] proposed a more general Lyapunov function, introducing an exponential term to accelerate the convergence rate of the system.

In recent years, machine learning has been widely used in the modeling and control of complex dynamic systems. For example, Wang and Li [44] used dynamic system deep learning (DSDL) to achieve interpretable predictions for chaotic systems. In situations where the spatial environment is uncertain, Jahanshahi and Zhu [45] applied machine learning and robotic grasping to improve accuracy and adaptability. In 2025, Zahedifar et al. [46] proposed the large language model controller (LLM-Controller), which can analyze unknown perturbations, unmodeled dynamics, and changing reference signals, and can adapt to new conditions without manual adjustments. These studies showed that machine learning can effectively deal with uncertainty in dynamic environments, which is one of the challenges of financial market regulation. Uncertainties and perturbations in chaotic systems can vary significantly over time. Traditional methods usually assumed that the uncertainty was confined to a fixed upper bound [47], which is not suitable for describing complex and dynamic uncertainties. But the adaptive characteristics of the RBF neural network (RBFNN) enable it to dynamically adjust its approximation ability, effectively responding to the fast-changing uncertainties in chaotic models. Hence, it is crucial to explore the predefined-time SMC approach with the RBFNN. The predefined-time stability theory and the approximation performance of the RBFNN were used to address the tracking problem of uncertain nonlinear models [48]. Liu et al. [49] adaptively estimated unknown perturbations to refine control accuracy. A neural controller was developed in [50]. Currently, there is limited related research on synchronization of chaotic systems. Since the controller employing the RBFNN can adjust the approximation for uncertainties and avoid unnecessary compensation, it can therefore regulate market disturbances in real-time in the financial market, thus reducing the cost of regulation and excessive policy intervention. Based on this, we consider designing a controller with the RBFNN to achieve synchronization in financial chaotic models, which better aligns with the practical demands.

Motivated by the previous discussion, this manuscript develops a novel FO financial model and an innovative predefined-time SMC strategy utilizing the RBFNN. This manuscript makes the following primary contributions:

1) Based on the current integer-order financial systems, a new three-dimensional FO chaotic model is established, and its dynamic behaviors are analyzed.

2) Based on the RBFNN, an innovative predefined-time SMC method is established to synchronize two FO chaotic models within a specified time.

3) To improves the efficiency of secure communication, the chaotic characteristics of the presented system are applied to image and voice encryption and the suggested control approach is successfully implemented in signal encryption.

The upcoming sections are structured in the subsequent way: Section 2 gives the basic definitions, stability theorems, and the framework of the RBFNN necessary for this paper. In Section 3, a novel FO financial chaotic model with non-constant demand elasticity is presented, and the nonlinear dynamic behaviors of the suggested model are explored. An innovative predefined-time control strategy based on the RBFNN is put forward to synchronize systems within a predefined time. Numerical analyses in Section 4 aim to validate the usefulness of the introduced controller. Section 5 applies the proposed system and the synchronization method to secure encryption. This paper finishes with a summary and final thoughts in Section 6.

## 2. Preliminaries

### 2.1. Definitions of fractional calculus

Given that the Caputo fractional derivative requires only starting conditions consistent with integer-order equations, it is more applicable to real-life situations. Therefore, this paper employs the Caputo definition for its analyses. The following definitions are adopted from reference [1].

**Definition 2.1.** *Euler's gamma function, a key component of fractional calculus, is expressed as*

$$\Gamma(s) = \int_0^{\infty} \mathrm{t}^{s-1} e^{-t} \mathrm{d}t \tag{2.1}$$

**Definition 2.2.** *$f(t)'s$ $\rho$th-order RL integral is identified as*

$$ {}^{RL}_{t_0}D_t^{-\rho} f(t) = \frac{1}{\Gamma(\rho)} \int_{t_0}^{t} \frac{f(\tau)}{(t-\tau)^{1-\rho}} \mathrm{d}\tau \tag{2.2}$$

*where $0 < \rho < 1$, and $t_0$ refers to the starting time.*

**Definition 2.3.** *$f(t)'s$ $\rho$th-order Caputo derivative is described by*

$$ {}^{C}_{t_0}D_t^{\rho} f(t) = \begin{cases} \frac{1}{\Gamma(q-\rho)} \int_{t_0}^{t} \frac{f^{(q)}(\tau)}{(t-\tau)^{\rho-q+1}} d\tau, & q-1 < \rho < q, \\ \frac{d^q f(t)}{dt^q}, & \rho = q, \end{cases} \tag{2.3}$$

*where $q-1 < \rho < q, q \in N$, and $\Gamma(.)$ and $t_0$ are the same as above. Moreover, when $0 < \rho < 1$,*

$$ {}^{C}_{t_0}D_t^{\rho} f(t) = \frac{1}{\Gamma(1-\rho)} \int_{t_0}^{t} (t-\tau)^{-\rho} f'(\tau) d\tau \tag{2.4}$$

*2.2. Stability theorem of FO systems*

**Lemma 2.1.** *[51]. Considering the subsequent r-dimensional fractional-order model*

$$\frac{d^{\rho}x_i}{dt^{\rho}} = f_i(x_1, x_2, \ldots, x_r), i = 1, 2, \ldots, r, \tag{2.5}$$

*where* $0 < \rho < 1$*, if all eigenvalues* $\lambda$ *of the Jacobian matrix at the system's equilibrium points meet*

$$|arg(\lambda)| > \rho\pi/2, \tag{2.6}$$

*these points are locally asymptotic stability.*

**Property 2.1.** *[52]. If* $f(t) \in C^1[t_0, \infty)$ *and* $0 < \rho < 1$*, then*

$$D^{\rho}(I^{\rho}f(t)) = f(t) \tag{2.7}$$

**Property 2.2.** *[53]. If* $f(t) \in C^1[0, A]$ *and* $0 < \rho_1 + \rho_2 < 1$*, we have*

$$D^{\rho_1}(D^{\rho_2}f(t)) = D^{\rho_2}(D^{\rho_1}f(t)) = D^{\rho_1+\rho_2}f(t) \tag{2.8}$$

*2.3. RBF neural network*

Studies have confirmed that the RBFNN can approximate nonlinear functions with any required precision [54]. As shown in Figure 1, the RBFNN consists of a simple three-layer feedforward structure featuring one hidden layer. Every unit in this layer contains a radial basis function:

$$h_j(\boldsymbol{X}) = \exp\left(-\frac{\left\|\boldsymbol{X} - \boldsymbol{c}_j\right\|}{2b_j^2}\right), j = 1, 2, \cdots, m, \tag{2.9}$$

where $\boldsymbol{X}$ denotes the input vector, and $\boldsymbol{c}_j$ and $b_j$ denote the center vector and the width of the $j$-th unit in the hidden layer, respectively. The node's linear output value is:

$$y_i = \sum_{j=1}^{m} w_{ij}h_j = \boldsymbol{W}_i^{\mathrm{T}}\boldsymbol{H} \quad , i = 1, 2, \cdots, n, \tag{2.10}$$

where $\boldsymbol{W}_i$ means the weight vector. The training algorithm of the RBFNN is divided into two stages: parameter determination of the hidden layer and parameter determination of the output layer. Hidden layer parameters include the center and width. Centers are usually selected automatically in the input data, and determination methods include K-means clustering and orthogonal least squares. The width determines the extent of the extension of the basis function and is usually determined by the center distance method or the fixed width method. The parameters of the output layer are weights, and the determination methods include the least square method and gradient descent method. The selection of different algorithms depends on the characteristics of the data, and needs to be flexibly adapted to the actual condtions to achieve the best training effect. In this work, we use the RBFNN to estimate uncertain and disturbed terms. We follow the same principle, updating the weights using gradient descent but manually adjusting the values of the center and width, reducing the computational complexity.

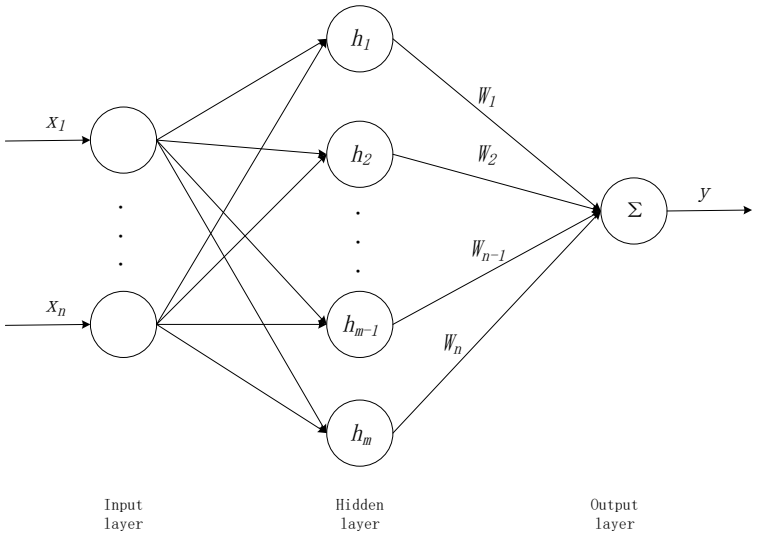


**Figure 1.** Topology of the RBFNN [24].

### *2.4. Predefined-time convergence and synchronization*

We analyze the following temporal system:

$$\dot{\boldsymbol{x}}(t) = \boldsymbol{f}(t, \boldsymbol{x}(t)), \tag{2.11}$$

where $\boldsymbol{x}$ indicates the state variable, and $\boldsymbol{f}$ is a nonlinear function with $\boldsymbol{f}(t, \boldsymbol{0}) = \boldsymbol{0}$.

**Definition 2.4.** *[39]. If the model (2.11) is fixed-time stable and the settling-time function $T(x_0)$ satisfies $T(x_0) \leq T_c$, it is said to be globally predefined-time stable, where $T_c$ is a bounded positive constant representing the specified time.*

**Lemma 2.2.** *[47]. For $n_i$, $\vartheta \in \mathcal{R}^+$, the subsequent inequalities are*

$$\begin{cases} \left(\sum_{i=1}^{m}|n_i|\right)^{\vartheta} \leq \sum_{i=1}^{m}|n_i|^{\vartheta}, 0 < \vartheta \leq 1 \\ m^{1-\vartheta}\left(\sum_{i=1}^{m}|n_i|\right)^{\vartheta} \leq \sum_{i=1}^{m}|n_i|^{\vartheta}, 1 \leq \vartheta < +\infty \end{cases} \tag{2.12}$$

**Lemma 2.3.** *For a positive constant $T_c > 0$, if an unbounded Lyapunov function $V(x)$ exists and meets*

$$\dot{V} \leqslant -\frac{\pi(1+\alpha)}{\alpha T_c l_2}\left(l_1 V^{\frac{1}{1+\alpha}} + l_2 V + l_3 V^{\frac{1+2\alpha}{1+\alpha}}\right) \tag{2.13}$$

*then the origin of (2.11) is globally predefined-time stable, where $0 < \alpha < 1$, $l_2 = 2\sqrt{l_1 l_3}$, and $T_c$ is a predefined time. We can call (2.13) a novel predefined-time Lyapunov sufficient condition.*

*Proof.* The function $T(x_0)$ adheres to

$$T(x_0) \leq \int_{V_0}^{0} \frac{dV}{-\frac{\pi(1+\alpha)}{\alpha T_c l_2}\left(l_1 V^{\frac{1}{1+\alpha}} + l_2 V + l_3 V^{\frac{1+2\alpha}{1+\alpha}}\right)}$$

$$
\begin{aligned}
&= \frac{\alpha T_c l_2}{\pi(1+\alpha)} \int_0^{V_0} \frac{dV}{l_1 V^{\frac{1}{1+\alpha}} \left(1 + \frac{l_2}{l_1} V^{\frac{\alpha}{1+\alpha}} + \frac{l_3}{l_1} V^{\frac{2\alpha}{1+\alpha}}\right)} \\
&= \frac{\alpha T_c l_2}{\pi(1+\alpha)} \frac{1+\alpha}{\alpha} \int_0^{V_0} \frac{dV^{\frac{\alpha}{1+\alpha}}}{l_1 \left(1 + \sqrt{\frac{l_3}{l_1}} V^{\frac{\alpha}{1+\alpha}}\right)^2} \\
&= \frac{\alpha T_c l_2}{\pi(1+\alpha)} \frac{1+\alpha}{\alpha} \frac{1}{\sqrt{l_1 l_3}} \int_0^{V_0} \frac{d\sqrt{\frac{l_3}{l_1}} V^{\frac{\alpha}{1+\alpha}}}{\left(1 + \sqrt{\frac{l_3}{l_1}} V^{\frac{\alpha}{1+\alpha}}\right)^2} \\
&\leq \frac{2T_c}{\pi} \int_0^{V_0} \frac{d\sqrt{\frac{l_3}{l_1}} V^{\frac{\alpha}{1+\alpha}}}{1 + \frac{l_3}{l_1} V^{\frac{2\alpha}{1+\alpha}}} \\
&= \frac{2T_c}{\pi} \left( arctan\left( \sqrt{\frac{l_3}{l_1}} V^{\frac{\alpha}{1+\alpha}} \right) |_0^{V_0} \right) \\
&\leq \frac{2T_c}{\pi} \frac{\pi}{2} \\
&\leq T_c
\end{aligned}
\tag{2.14}
$$

**Remark 2.1.** *Lemma 2.3 complies with Definition 2.4, and the convergence time, which remains unaffected by the initial values, can be specified by the users.*

## 3. Main results

### *3.1. A newly designed FO financial model*

#### 3.1.1. System description

Based on reference [9], the non-constant elasticity of demand $c + dxy/z$ was considered [15]:

$$
\begin{cases}
\dot{x} = z + (y - a)x \\
\dot{y} = 1 - by - x^2 \\
\dot{z} = -x - cz - dxy
\end{cases}
\tag{3.1}
$$

and a novel financial chaotic model incorporating two quadratic and one sextic nonlinear terms was presented [16]:

$$
\begin{cases}
\dot{x} = z + (y - a)x \\
\dot{y} = 1 - by - bx^2 - cx^6 \\
\dot{z} = -x - z
\end{cases}
\tag{3.2}
$$

Since the non-constant elasticity of demand is more suitable for the financial market, we develop a novel financial system by considering it based on (3.2):

$$\begin{cases} \dot{x} = z + (y - a)x \\ \dot{y} = 1 - by - bx^2 - cx^6 \\ \dot{z} = -x - dz - exy \end{cases} \tag{3.3}$$

where state variables symbolize the interest rate, investment demand, and price index, $a$ denotes the saving amount, which influences the market interest rate's responsiveness to investment demand—a larger value indicates a higher savings rate, leading to smoother fluctuations in the interest rate. $b$ is the cost per investment, reflecting the inhibitory effect of investment costs on demand—a higher value makes financing more difficult, thus limiting investment demand. $c$ represents the coefficient of higher-order nonlinear effect, which measures the market's sensitivity to extreme financial volatility, such as a crisis—a higher value indicates a more volatile market. $d$ is the natural decay rate of $z$, determining how quickly the market adjusts to price changes—a higher value means a faster market response to shifts in supply and demand. and $e$ signifies the nonlinear amplification factor, measuring the extent to which interest rates and investment demand influence price changes—a larger value means the market demand is more sensitive to price fluctuations. Compared to model (3.2), model (3.3) modifies the demand elasticity from 1 to $d + exy/z$. The demand elasticity gauges how the quantity demanded reacts to price fluctuations, when the elasticity equals 1. Demand is perfectly proportional to price changes. However, this assumes an overly idealized system that ignores the dynamic evolution, feedback mechanisms, and nonlinear shocks. In real markets, demand elasticity is dynamically adjusted by the market environment. As the interest rate rises, the available funds of enterprises and individuals become more constrained, making demand more sensitive to changes in prices. Similarly, in environments with high investment demand, resource scarcity increases and demand becomes more sensitive to price fluctuations. When prices rise, many consumers may shift to substitutes or reduce overall demand, weakening the impact of price changes on purchasing power. In model (3.3), we can adjust the parameters $d$ and $e$ to suit different markets. To test the rationality, we choose the six-month interbank offered rate, the total investment and the average consumer price percentage change rate from 1980 to 2011 in Japan, to express the three state variables. The data are sourced from EconStats. Let $d = 0.9, e = 0.06$, and we use the above data to calculate the mean square error (MSE) of fixed and dynamic demand elasticity price index change. The former is 0.0028, while the letter is 0.0027. We also use the Diebold-Mariano (DM) test to compare the error differences. The results show a DM statistic of 3.5829 and a p-value of 0.0012, which is significantly less than 0.05, indicating that the dynamic model more effectively captures economic dynamics.

In the following analysis, we set the parameter values as $(a, b, c, d, e) = (4.4, 0.1, 0.2, 0.9, 0.06)$, where these values are chosen based on economic theories and market characteristics. $a = 4.4$ represents a high savings rate, corresponding to economies with significant capital accumulation. $b = 0.1$ reflects relatively easy financing conditions, resembling markets with accommodative monetary policies. $c = 0.2$ accounts for nonlinear effects in investment demand, reflecting the impact of extreme events on the market. $d = 0.9$ corresponds to the rapid price adjustments of modern financial markets, while $e = 0.06$ ensures a moderate elasticity impact. We then demonstrate the superiority of this system from the perspective of chaotic complexity.

The system (3.1) is chaotic when $(a, b, c, d) = (1, 0.1, 1, 0.1)$. When the starting state $X(0) = (0.4, 0.2, 0.5)$ and $T = 1E5$, the Lyapunov exponents (LEs) are computed as $L_1 = 0.16277$, $L_2 = 0$, and $L_3 = -0.43970$, and the Kaplan-Yorke (KY) dimension is calculated as follows:

$$D_{KY} = 2 + \frac{L_1 + L_2}{\mid L_3 \mid} = 2.3702 \tag{3.4}$$

The system (3.2) is chaotic when $(a, b, c) = (7.6, 0.1, 0.2)$. When the starting state $X(0) = (0.4, 0.2, 0.5)$ and $T = 1E5$, the LEs are obtained as $L_1 = 0.12299$, $L_2 = 0$, and $L_3 = -0.39478$, and the KY dimension is calculated as follows:

$$D_{KY} = 2 + \frac{L_1 + L_2}{\mid L_3 \mid} = 2.3115 \tag{3.5}$$

Similarly, when $(a, b, c, d, e) = (4.4, 0.1, 0.2, 0.9, 0.06)$, the starting state $X(0) = (0.4, 0.2, 0.5)$ and $T = 1E5$, the LEs of the new financial system (3.3) are calculated as $L_1 = 0.16702$, $L_2 = 0$, and $L_3 = -0.32872$. Also, the KY dimension is calculated as follows:

$$D_{KY} = 2 + \frac{L_1 + L_2}{\mid L_3 \mid} = 2.5081 \tag{3.6}$$

Table 1 presents a comparison of the three financial models mentioned above.

**Table 1.** Comparison of the three financial chaotic models.

| Chaotic systems | Maximal Lyapunov Exponent (MLE) | KY Dimension |
|---|---|---|
| Yang financial system (3.1) | $L_1 = 0.16277$ | $D_{KY} = 2.3702$ |
| Subartini financial system (3.2) | $L_1 = 0.12299$ | $D_{KY} = 2.3115$ |
| New financial system (3.3) | $L_1 = 0.16702$ | $D_{KY} = 2.5081$ |

**Remark 3.1.** *From Table 1, it is evident that the novel financial chaotic model (3.3) characterized by the largest Lyapunov exponent, exhibits greater chaotic complexity compared to the other two chaotic systems.*

Because of the strong historical dependence of financial variables, the financial markets often exhibit long memory effects. In order to better capture this feature, we extend the integer-order financial chaotic model to an FO financial chaotic system:

$$\begin{cases} D^{\rho}x = z + (y - a)x \\ D^{\rho}y = 1 - by - bx^2 - cx^6 \\ D^{\rho}z = -x - dz - exy \end{cases} \tag{3.7}$$

where $\rho$ is the fractional order. The following sections of this paper will center on this model (3.7).

### 3.1.2. Dynamic behaviors

Since the stability of an equilibrium point is influenced by both the order and system parameters, it is essential to explore how their variations affect the system. In this part, the predictor-corrector method [55] is employed to solve FO differential equations.

1) The influence of order $\rho$

For the sake of analysis, we fix $a = 4.4, b = 0.1, c = 0.2, d = 0.9, e = 0.06$, along with the starting values $X(0) = (0.4, 0.2, 0.5)$. When $\rho$ alters, the bifurcation diagram and the Lyapunov exponent spectrum (LEs) are shown in Figure 2.

The bifurcation diagram shows how the system's solutions evolve as a parameter varies. When the solutions gather around a point or within a small range, the system is stable, if the solutions form clusters, the model exhibits periodic behavior. Conversely, an irregular and random distribution of solutions indicate chaotic behavior. MLE is used to measure whether the system's trajectory will rapidly separate over time. When MLE $< 0$, the model is stable, when MLE $= 0$, the model is in a boundary period or a critical stable state, and when MLE $> 0$, the model is chaotic. From Figure 2, we observe that the two diagrams align, equilibrium points remain stable when $\rho \in [0.7, 0.78]$, the model behaves periodically when $\rho \in [0.82, 0.95]$, while chaotic behavior occurs for $\rho \in [0.78, 0.82]$ and $\rho \in [0.95, 1]$. Figure 3 depicts the time series and phase diagrams for $\rho = 0.8$ and $\rho = 0.98$, respectively, showing that their chaotic characteristics are distinct. In Figure 3(a), although the oscillations of $x$ appear regular, small variations emerge over time. Figure 3(c) reveals substantial changes in the oscillation frequency and fluctuation magnitude. In Figure 3(b), the system's trajectory is complex yet retains some degree of regularity, while in Figure 3(d), the trajectory becomes more dispersed and widely spread, displaying complete disorder. These observations suggest that the system exhibits stronger chaos at $\rho = 0.98$. There are several other ways to characterize chaos, such as the 0-1 test and the Poincaré map. The 0-1 test helps determine whether the model operates in a chaotic regime. If the system's trajectories in the $p - s$ plane are bounded, the model is quasiperiodic, and if the trajectories are Brownian-like, the model exhibits chaos. In Figure 4(a), the irregular pattern suggests that the model is chaotic. The Poincaré map is defined by the motion of trace lines in the phase space. If the points on the cross-section are isolated, the system is stable, if there are only a few discrete points, the system is periodic, and if points are densely distributed, the model is chaotic. In Figure 4(b), the dense, irregular, and partially random distribution of points suggests that the system exhibits chaotic dynamics. The simulation results show that the FO system can exhibit richer dynamic behaviors and describe the complex evolution of financial markets more accurately.

2) The influence of parameter $a$

We fix $b = 0.1, c = 0.2, d = 0.9, e = 0.06$, and $\rho = 0.98$. When $a$ alters from 4 to 6, the bifurcation diagram and the LEs are shown in Figure 5. The system (3.7) shows chaotic behavior when $a \in [4, 5.4]$, and behaves periodically when $a \in [5.4, 6]$. Saving counts play a crucial role in chaotic and cyclical financial systems: when $a$ is low, capital liquidity increases, but stability decreases, making the market more sensitive to external shocks and prone to enter a chaotic state, which leads to the instability of economic growth and may lead to financial crisis. As $a$ increases, the market interest rate becomes more stable, promoting stable capital accumulation and the system stabilizes. Choosing an appropriate value for $a$ can better manage risks and maintain sustainable economic growth.

3) The influence of parameter $b$

We fix $a = 4.4, c = 0.2, d = 0.9, e = 0.06$, and $\rho = 0.98$. When $b$ alters from 0 to 0.18, the bifurcation diagram and the LEs are shown in Figure 6. It is observed that the model (3.7) is in a periodic state when $b \in [0, 0.08]$, enters chaos when $b \in [0.08, 0.12]$, and finally tends to a periodic state when $b \in [0.12, 0.18]$. Investment costs affect chaotic and cyclical financial systems. When $b$ is low, financing is easy and investment fluctuations are minimal. As $b$ increases, capital flow becomes

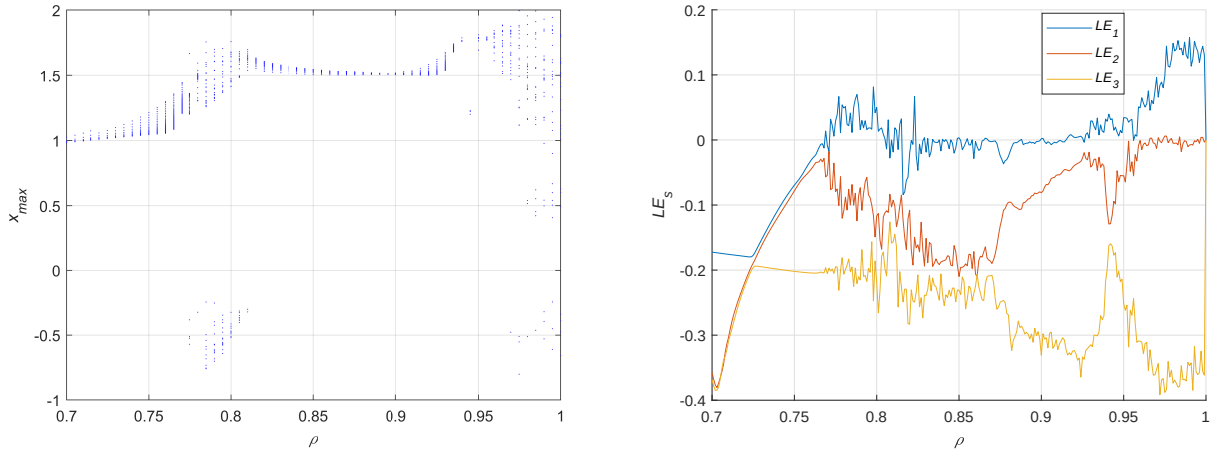


(a) Bifurcation diagram relative to $\rho$

(b) LE diagram relative to $\rho$

**Figure 2.** Bifurcation and LE diagrams of model 3.7 at $(a, b, c, d, e) = (4.4, 0.1, 0.2, 0.9, 0.06)$ and $\rho \in [0.7, 1]$.

unbalanced, and investment behavior becomes more uncertain, leading to unpredictable market behavior and increasing the risk of a financial crisis. Once $b$ exceeds a certain threshold, investment becomes constrained, and the market tends to stabilize. Businesses are better able to allocate resources, reducing financial turbulence. Choosing an appropriate value for $b$ is crucial to maintaining a stable and dynamic financial environment.

4) The influence of parameter $c$

We fix $a = 4.4, b = 0.1, d = 0.9, e = 0.06$, and $\rho = 0.98$. When $c$ alters from 0 to 1, the bifurcation diagram and the LEs are shown in Figure 7. It is clear that the model (3.7) exhibits a positive largest Lyapunov exponent and shows chaotic dynamics within all ranges. The coefficient of higher-order nonlinear effects affect chaotic systems, which indicates that the market is subject to extreme financial volatility. To mitigate such volatility, financial regulation can be strengthened to reduce high leverage and speculation.

5) The influence of parameter $d$

We fix $a = 4.4, b = 0.1, c = 0.2, e = 0.06$, and $\rho = 0.98$. When $d$ alters from 0 to 1, the bifurcation diagram and the LEs are shown in Figure 8. The system (3.7) is chaotic when $d \in [0, 0.14]$ and $d \in [0.79, 1]$, and behaves periodically when $d \in [0.14, 0.79]$. Demand elasticity affects price stability and market dynamics. Parameter $d$ represents the rate at which the market adapts to price changes. When $d$ is too small, the delayed response may cause large price fluctuations. When $d$ is too large, excessive fluctuations may lead to chaos, leading to speculative bubbles and financial crises. In a cyclical financial system, firms can more structurally adjust their pricing strategies to make predictable investment plans. Therefore, choosing an appropriate value for $d$ is crucial for maintaining market responsiveness and controlling market stability.

6) The influence of parameter $e$

We fix $a = 4.4, b = 0.1, c = 0.2, d = 0.9$, and $\rho = 0.98$. When $e$ alters from 0 to 0.2, the bifurcation

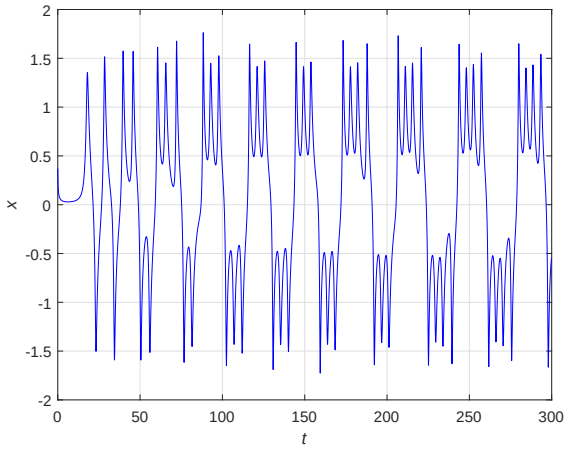


(a) Time history diagram when $\rho = 0.8$

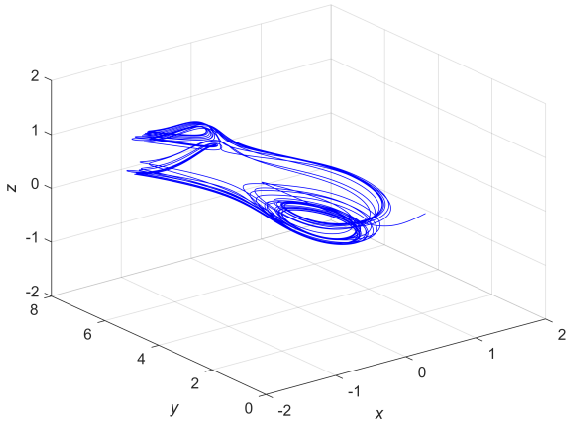


(b) Phase diagram when $\rho = 0.8$

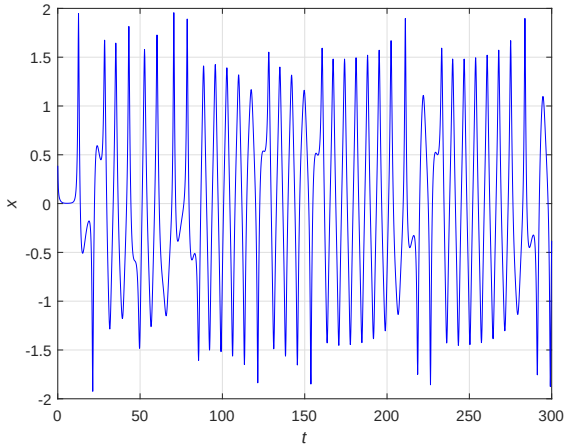


(c) Time history diagram when $\rho = 0.98$

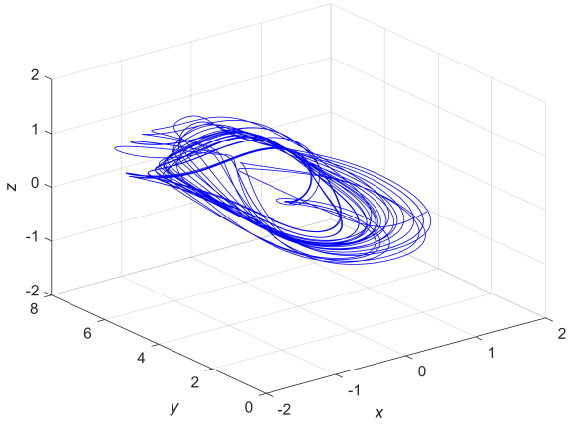


(d) Phase diagram when $\rho = 0.98$

**Figure 3.** Time history and phase diagrams of model 3.7.

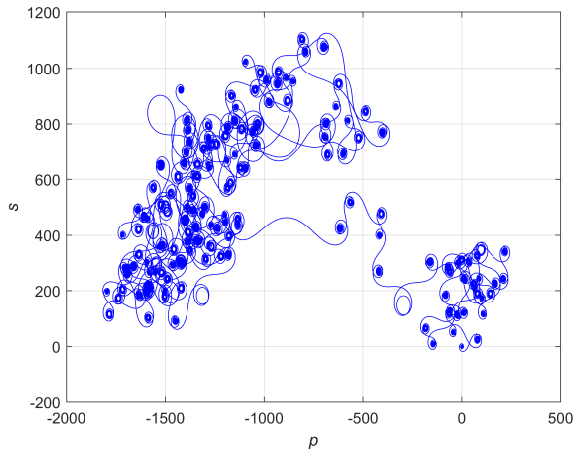


(a) 0-1 test diagram when $\rho = 0.8$

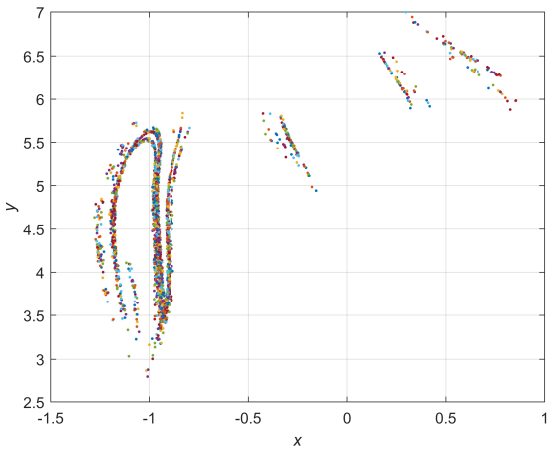


(b) Poincaré diagram when $\rho = 0.98$

**Figure 4.** 0-1 test and Poincaré diagram of model 3.7.

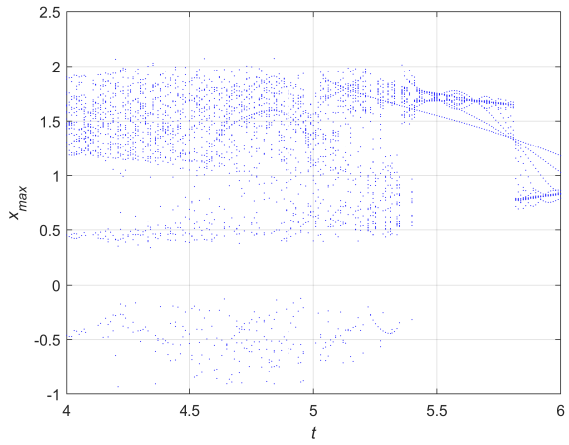


(a) Bifurcation diagram relative to $a$

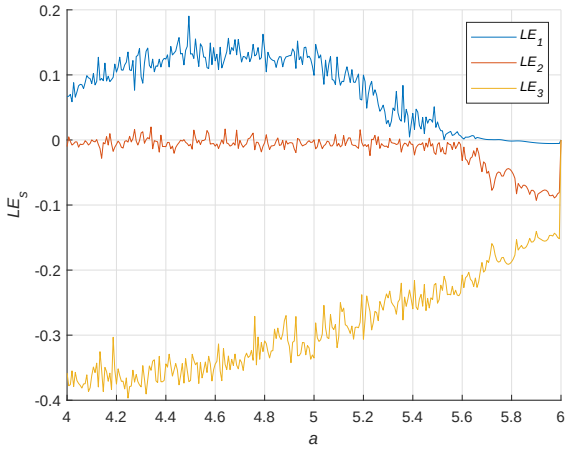


(b) LE diagram relative to $a$

**Figure 5.** Bifurcation and LE diagrams of model (3.7) at $(b, c, d, e) = (0.1, 0.2, 0.9, 0.06)$ and $a \in [4, 6]$.

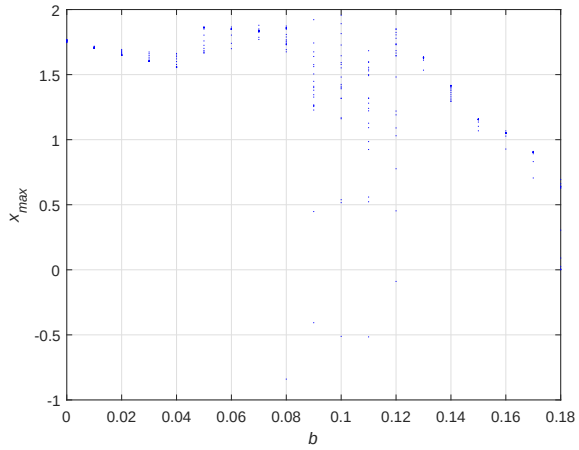


(a) Bifurcation diagram relative to $b$

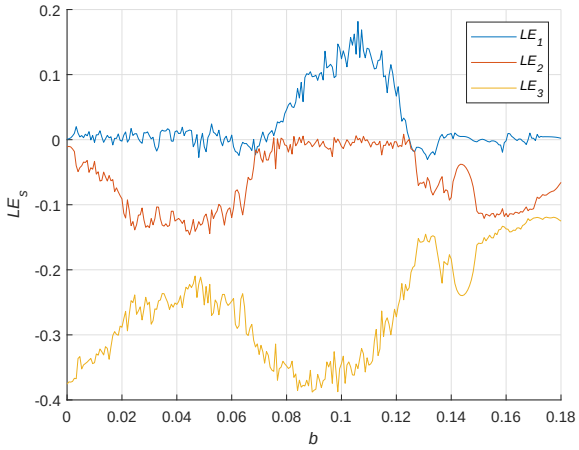


(b) LE diagram relative to $b$

**Figure 6.** Bifurcation and LE diagrams of model (3.7) at $(a, c, d, e) = (4.4, 0.2, 0.9, 0.06)$ and $b \in [0, 0.18]$.

diagram and the LEs are shown in Figure 9. The model (3.7) is in a periodic state when $e \in [0, 0.03]$ and $e \in [0.1, 0.2]$, and is chaotic when $e \in [0.03, 0.1]$. Parameter $e$ represents the market's sensitivity to interest rates and investment demand. If $e$ is too small, price fluctuates are minimal, and if $e$ is too large, the price fluctuations are significant but regular. In a chaotic financial system, high sensitivity amplifies the unpredictability of markets, which can lead to speculative bubbles or market crashes. In a cyclical financial system, moderate sensitivity allows for a smooth transition between economic cycles. Therefore, selecting an appropriate value for $e$ can stabilize markets by allowing them to react in a controlled way.

These simulation results show that the system's dynamic behavior is influenced by variations in both the order and parameters. By understanding how these parameters affect the market volatility, financial

institutions can better optimize their decisions, and regulators can formulate appropriate regulatory strategies to maintain market stability and prevent potential financial crises.

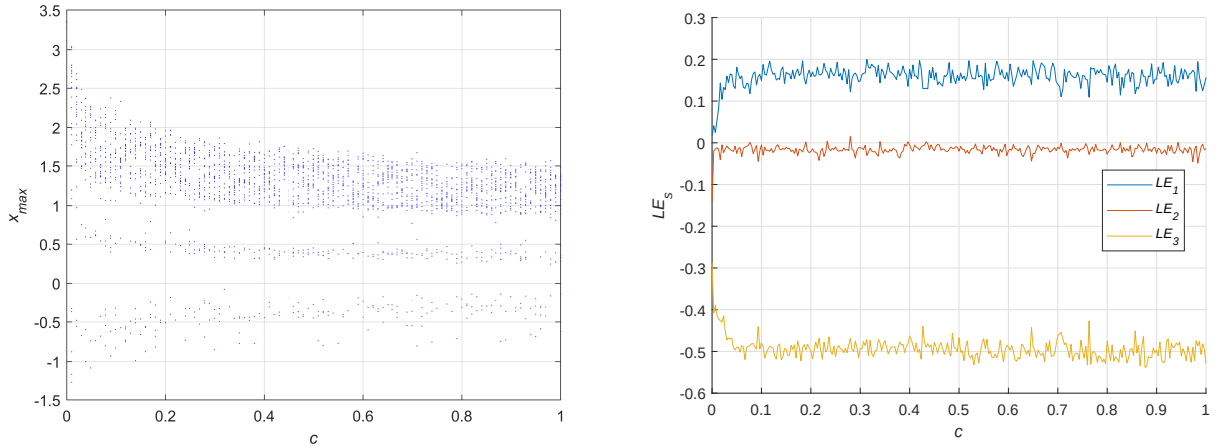


(a) Bifurcation diagram relative to $c$

(b) LE diagram relative to $c$

**Figure 7.** Bifurcation and LE diagrams of model (3.7) at $(a, b, d, e) = (4.4, 0.1, 0.9, 0.06)$ and $c \in [0, 1]$.

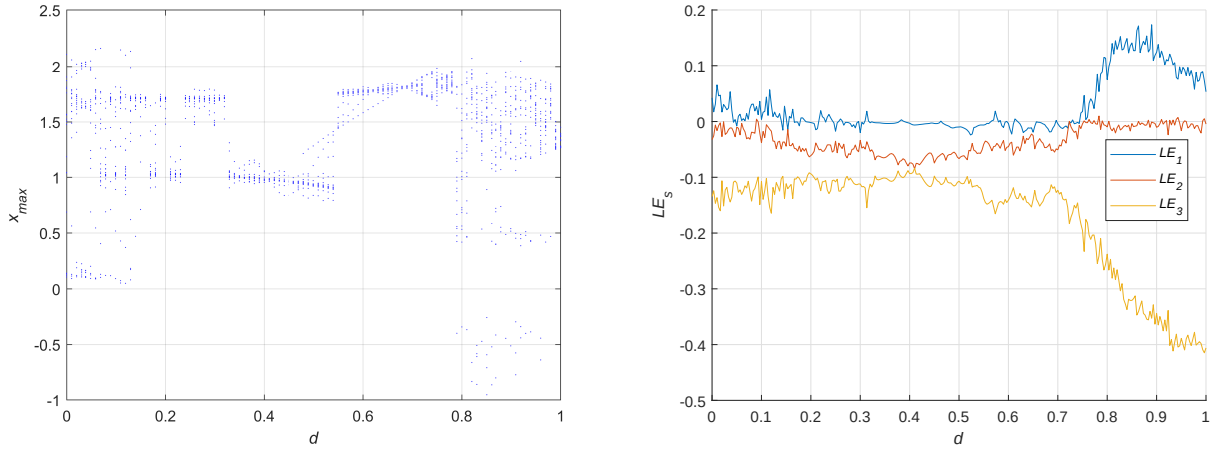


(a) Bifurcation diagram relative to $d$

(b) LE diagram relative to $d$

**Figure 8.** Bifurcation and LE diagrams of model (3.7) at $(a, b, c, e) = (4.4, 0.1, 0.2, 0.06)$ and $d \in [0, 1]$.

### *3.2. Predefined-time synchronization method for chaotic models*

In the following part, we first develop a new sliding surface guided by the new unbounded Lyapunov function (2.13). Then, a controller containing the estimator of uncertainties and external disturbances is introduced. Finally, this proposed method ensures that the error model converge and the master-slave systems achieve synchronization within a predefined time.

We analyze the subsequent $r$-dimensional nonlinear FO master and slave models, as described by

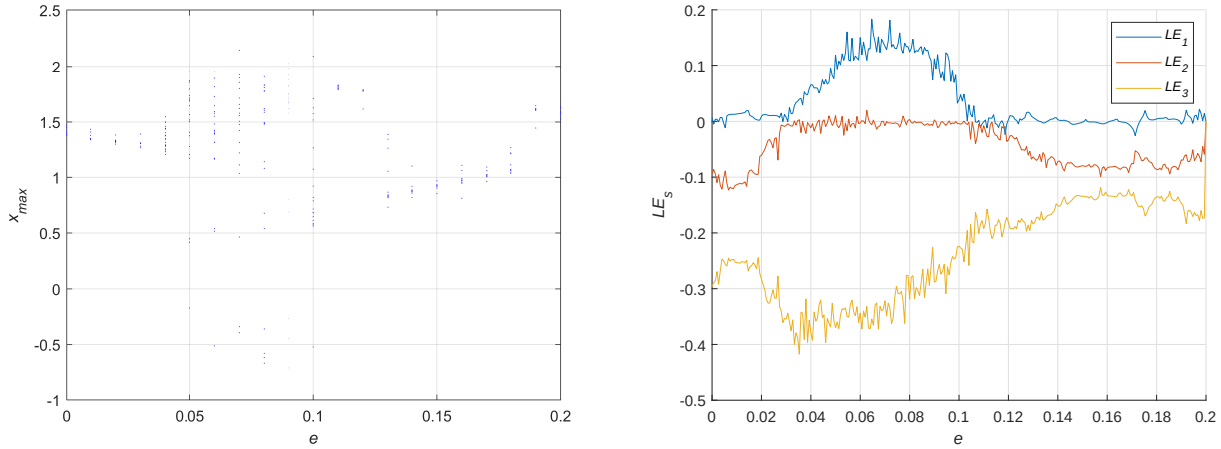


(a) Bifurcation diagram relative to $e$

(b) LE diagram relative to $e$

**Figure 9.** Bifurcation and LE diagrams of model (3.7) at $(a, b, c, d) = (4.4, 0.1, 0.2, 0.9)$ and $e \in [0, 0.2]$.

Eqs (3.8) and (3.9).

$$D_t^{\rho} x_i = f_i(\boldsymbol{x}, t), i = 1, 2, \ldots, r \tag{3.8}$$

$$D_t^{\rho} y_i = g_i(\boldsymbol{y}, t) + D_i(\boldsymbol{y}, t) + u_i(t), i = 1, 2, \ldots, r \tag{3.9}$$

where $\rho$ symbolizes the fractional order, $\boldsymbol{x} = (x_1, x_2, \ldots, x_r)^T$, and $\boldsymbol{y} = (y_1, y_2, \ldots, y_r)^T$ are state variables, and $f_i(\boldsymbol{x}, t)$ and $g_i(\boldsymbol{y}, t)$ are nonlinear differentiable functions. In addition, $D_i(\boldsymbol{y}, t) = \Delta g_i(\boldsymbol{y}, t) + d_i(t)$, $\Delta g_i(\boldsymbol{y}, t)$ are the uncertainties, $d_i(t)$ are the external interferences, $u_i(t)$ are the control inputs to be determined, and $i = 1, 2, \ldots, r$.

We describe the synchronization error as $e_i = x_i - y_i$, so the error model is given by:

$$D_t^{\rho} e_i = f_i(\boldsymbol{x}, t) - g_i(\boldsymbol{y}, t) - D_i(\boldsymbol{y}, t) - u_i(t), i = 1, 2, \ldots, r \tag{3.10}$$

We will then develop a predefined-time SMC approach with an RBFNN aimed at maintaining the stability of (3.10) within a specified time.

### 3.2.1. Sliding surface

To stabilize the error model (3.10), we design the following sliding surface:

$$s_i = D^{\rho-1} e_i + D^{\rho-2} \left( d_1 sign(e_i) |e_i|^{\frac{1}{1+\eta_1}} + d_2 sign(e_i) |e_i|^{\frac{1+2\eta_1}{1+\eta_1}} + d_3 e_i + d_4 sign(e_i) \right) \tag{3.11}$$

where $\rho \in (0,1)$, $\eta_1 \in (0,1)$, $d_4 > 0$, $d_1 = \frac{\pi(1+\eta_1)}{2\eta_1 T_1}$, $d_2 = \frac{\pi(1+\eta_1)}{2\eta_1 T_1 r^{\frac{-\eta_1}{1+\eta_1}}}$, $d_3 = \frac{\pi(1+\eta_1)}{\eta_1 T_1}$. When the system (3.10) enters the sliding mode, it meets $s_i = 0$ and $\dot{s}_i = 0$. So we have:

$$D^{\rho} e_i = -D^{\rho-1} \left( d_1 sign(e_i) |e_i|^{\frac{1}{1+\eta_1}} + d_2 sign(e_i) |e_i|^{\frac{1+2\eta_1}{1+\eta_1}} + d_3 e_i + d_4 sign(e_i) \right) \tag{3.12}$$

**Theorem 3.1.** *When the sliding surface (3.11) is applied, the error system (3.10) stabilizes and converges to zero within a predefined time $T_1$.*

*Proof.* Choose the Lyapunov function as follows:

$$V_1 = \sum_{i=1}^{r} |e_i(t)| \tag{3.13}$$

The derivative of $V_1(t)$ is

$$\begin{aligned}
\dot{V}_1 &= \sum_{i=1}^{r} sign\,(e_i)\,\dot{e}_i \\
&= \sum_{i=1}^{r} sign\,(e_i)\left(D^{1-\rho}\left(D^{\rho}e_i\right)\right) \\
&= \sum_{i=1}^{r} sign\,(e_i)\left(D^{1-\rho}\left(-D^{\rho-1}\left(d_1 sign\,(e_i)\,|e_i|^{\frac{1}{1+\eta_1}} + d_2 sign\,(e_i)\,|e_i|^{\frac{1+2\eta_1}{1+\eta_1}} + d_3 e_i + d_4 sign\,(e_i)\right)\right)\right) \\
&= \sum_{i=1}^{r} sign\,(e_i)\left(-d_1 sign\,(e_i)\,|e_i|^{\frac{1}{1+\eta_1}} - d_2 sign\,(e_i)\,|e_i|^{\frac{1+2\eta_1}{1+\eta_1}} - d_3 e_i - d_4 sign\,(e_i)\right) \\
&\le \sum_{i=1}^{r} sign\,(e_i)\left(-d_1 sign\,(e_i)\,|e_i|^{\frac{1}{1+\eta_1}} - d_2 sign\,(e_i)\,|e_i|^{\frac{1+2\eta_1}{1+\eta_1}} - d_3 e_i\right) \\
&= -d_1 \sum_{i=1}^{r} |e_i|^{\frac{1}{1+\eta_1}} - d_2 \sum_{i=1}^{r} |e_i|^{\frac{1+2\eta_1}{1+\eta_1}} - d_3 \sum_{i=1}^{r} |e_i| \\
&\le -d_1 \left(\sum_{i=1}^{r} |e_i|\right)^{\frac{1}{1+\eta_1}} - d_2 r^{1-(\frac{1+2\eta_1}{1+\eta_1})} \left(\sum_{i=1}^{r} |e_i|\right)^{\frac{1+2\eta_1}{1+\eta_1}} - d_3 \left(\sum_{i=1}^{r} |e_i|\right) \\
&= -d_1 V_1^{\frac{1}{1+\eta_1}} - d_2 r^{\frac{-\eta_1}{1+\eta_1}} V_1^{\frac{1+2\eta_1}{1+\eta_1}} - d_3 V_1 \\
&= -\frac{\pi(1+\eta_1)}{2\eta_1 T_1} V_1^{\frac{1}{1+\eta_1}} - \frac{\pi(1+\eta_1)}{2\eta_1 T_1 r^{\frac{-\eta_1}{1+\eta_1}}} r^{\frac{-\eta_1}{1+\eta_1}} V_1^{\frac{1+2\eta_1}{1+\eta_1}} - \frac{\pi(1+\eta_1)}{\eta_1 T_1} V_1 \\
&= -\frac{\pi(1+\eta_1)}{2\eta_1 T_1}\left(V_1^{\frac{1}{1+\eta_1}} + 2V_1 + V_1^{\frac{1+2\eta_1}{1+\eta_1}}\right)
\end{aligned} \tag{3.14}$$

This fulfills Lemma 2.3. Thus, the state trajectories will approach zero in the predefined time $T_1$.

3.2.2. Controller design with the RBFNN

To achieve predefined-time synchronization, we create a controller as follows:

$$u_i = f_i - g_i - \widehat{D}_i + D^{\rho-1}\left(d_1 sign\,(e_i)\,|e_i|^{\frac{1}{1+\eta_1}} + d_2 sign\,(e_i)\,|e_i|^{\frac{1+2\eta_1}{1+\eta_1}} + d_3 e_i + d_4 sign\,(e_i)\right)$$

$$+ d_5 sign(s_i) |s_i|^{\frac{1}{1+\eta_2}} + d_6 sign(s_i) |s_i|^{\frac{1+2\eta_2}{1+\eta_2}} + d_7 s_i + d_8 sign(s_i) \tag{3.15}$$

where $\rho \in (0,1)$, $\eta_1 \in (0,1)$, $\eta_2 \in (0,1)$, $d_4, d_8 > 0$, $d_1 = \frac{\pi(1+\eta_1)}{2\eta_1 T_1}$, $d_2 = \frac{\pi(1+\eta_1)}{2\eta_1 T_1 r^{\frac{-\eta_1}{1+\eta_1}}}$, $d_3 = \frac{\pi(1+\eta_1)}{\eta_1 T_1}$, $d_5 = \frac{\pi(1+\eta_2)}{2\eta_2 T_2}$, $d_6 = \frac{\pi(1+\eta_2)}{2\eta_2 T_2 r^{\frac{-\eta_2}{1+\eta_2}}}$, $d_7 = \frac{\pi(1+\eta_2)}{\eta_2 T_2}$. In addition, $\widehat{D}_i(\boldsymbol{y}, t)$ represents the approximation of $D_i(\boldsymbol{y}, t)$, we let $\tilde{\boldsymbol{W}}_{\boldsymbol{i}} = \hat{\boldsymbol{W}}_{\boldsymbol{i}} - \boldsymbol{W}_{\boldsymbol{i}}^{*}$, where $\boldsymbol{W}_{\boldsymbol{i}}^{*}$ denotes the ideal weight, $\hat{\boldsymbol{W}}_{\boldsymbol{i}}$ is its approximation, and $\tilde{\boldsymbol{W}}_{\boldsymbol{i}}$ means the error between $\hat{\boldsymbol{W}}_{\boldsymbol{i}}$ and $\boldsymbol{W}_{\boldsymbol{i}}^{*}$. The adaptive law is defined as follows:

$$\dot{\widehat{\boldsymbol{W}}}_i = -\tau_i sign(s_i) \boldsymbol{H}, i = 1, 2, \ldots, r \tag{3.16}$$

where $\tau_i$ are positive constants.

**Theorem 3.2.** *Consider the controller (3.15) and the adaptive law (3.16). The error model (3.10) will converge to the sliding surface (3.11).*

*Proof.* Choose the Lyapunov function as follows:

$$V_2 = \sum_{i=1}^{r} |s_i(t)| + \sum_{i=1}^{r} \frac{1}{2\tau_i} \tilde{\boldsymbol{W}}_i^T \tilde{\boldsymbol{W}}_i \tag{3.17}$$

The derivative of $V_2(t)$ is

$$\begin{aligned}
\dot{V}_2 &= \sum_{i=1}^{r} sign(s_i) \dot{s}_i + \sum_{i=1}^{r} \frac{1}{\tau_i} \tilde{\boldsymbol{W}}_i^T \dot{\tilde{\boldsymbol{W}}}_i \\
&= \sum_{i=1}^{r} sign(s_i) \left( D^{\rho} e_i + D^{\rho-1} \left( d_1 sign(e_i) |e_i|^{\frac{1}{1+\eta_1}} + d_2 sign(e_i) |e_i|^{\frac{1+2\eta_1}{1+\eta_1}} + d_3 e_i + d_4 sign(e_i) \right) \right) + \\
&\quad \sum_{i=1}^{r} \frac{1}{\tau_i} \tilde{\boldsymbol{W}}_i^T \dot{\hat{\boldsymbol{W}}}_i \\
&= \sum_{i=1}^{r} sign(s_i) \left( f_i - g_i - D_i - u_i + D^{\rho-1} \left( d_1 sign(e_i) |e_i|^{\frac{1}{1+\eta_1}} + d_2 sign(e_i) |e_i|^{\frac{1+2\eta_1}{1+\eta_1}} + d_3 e_i + d_4 sign(e_i) \right) \right) \\
&\quad + \sum_{i=1}^{r} \frac{1}{\tau_i} \tilde{\boldsymbol{W}}_i^T \dot{\hat{\boldsymbol{W}}}_i \\
&= \sum_{i=1}^{r} sign(s_i) \left( -D_i + \widehat{D}_i - d_5 sign(s_i) |s_i|^{\frac{1}{1+\eta_2}} - d_6 sign(s_i) |s_i|^{\frac{1+2\eta_2}{1+\eta_2}} - d_7 s_i - d_8 sign(s_i) \right) + \\
&\quad \sum_{i=1}^{r} \frac{1}{\tau_i} \tilde{\boldsymbol{W}}_i^T \dot{\hat{\boldsymbol{W}}}_i \\
&= \sum_{i=1}^{r} sign(s_i) \left( \tilde{\boldsymbol{W}}_i^{\mathrm{T}} \boldsymbol{H} - \varepsilon - d_5 sign(s_i) |s_i|^{\frac{1}{1+\eta_2}} - d_6 sign(s_i) |s_i|^{\frac{1+2\eta_2}{1+\eta_2}} - d_7 s_i - d_8 sign(s_i) \right) + \\
&\quad \sum_{i=1}^{r} \frac{1}{\tau_i} \tilde{\boldsymbol{W}}_i^T \left( -\tau_i sign(s_i) \boldsymbol{H} \right)
\end{aligned}$$

$$
\begin{aligned}
&= \sum_{i=1}^{r} sign(s_i)\left(-\varepsilon - d_5 sign(s_i)|s_i|^{\frac{1}{1+\eta_2}} - d_6 sign(s_i)|s_i|^{\frac{1+2\eta_2}{1+\eta_2}} - d_7 s_i - d_8 sign(s_i)\right) + \sum_{i=1}^{r} sign(s_i)\widetilde{\boldsymbol{W}}_i^{\mathrm{T}}\boldsymbol{H} - \\
&\quad \sum_{i=1}^{r} sign(s_i)\widetilde{\boldsymbol{W}}_i^{\mathrm{T}}\boldsymbol{H} \\
&= \sum_{i=1}^{r} sign(s_i)\left(-\varepsilon - d_5 sign(s_i)|s_i|^{\frac{1}{1+\eta_2}} - d_6 sign(s_i)|s_i|^{\frac{1+2\eta_2}{1+\eta_2}} - d_7 s_i - d_8 sign(s_i)\right) \\
&\leq \sum_{i=1}^{r} sign(s_i)\left(-d_5 sign(s_i)|s_i|^{\frac{1}{1+\eta_2}} - d_6 sign(s_i)|s_i|^{\frac{1+2\eta_2}{1+\eta_2}} - d_7 s_i\right) \\
&= \sum_{i=1}^{r}\left(-d_5|s_i|^{\frac{1}{1+\eta_2}} - d_6|s_i|^{\frac{1+2\eta_2}{1+\eta_2}} - d_7|s_i|\right)
\end{aligned} \tag{3.18}
$$

where $\varepsilon$ is the network approximation error. Under this offered controller and adaptive law, the master (3.8) and slave system (3.9) will achieve synchronization.

**Theorem 3.3.** *Consider the controller (3.15) and the adaptive law (3.16). The error model (3.10) will converge to the sliding surface (3.11) within a predefined time $T_2$.*

*Proof.* Choose the Lyapunov function as follows:

$$
V_3 = \sum_{i=1}^{r}|s_i(t)| \tag{3.19}
$$

The derivative of $V_3(t)$ is

$$
\begin{aligned}
\dot{V}_3 &= \sum_{i=1}^{r} sign(s_i)\,\dot{s}_i \\
&= \sum_{i=1}^{r} sign(s_i)\left(D^{\rho}e_i + D^{\rho-1}\left(d_1 sign(e_i)|e_i|^{\frac{1}{1+\eta_1}} + d_2 sign(e_i)|e_i|^{\frac{1+2\eta_1}{1+\eta_1}} + d_3 e_i + d_4 sign(e_i)\right)\right) \\
&= \sum_{i=1}^{r} sign(s_i)\left(f_i - g_i - D_i - u_i + D^{\rho-1}\left(d_1 sign(e_i)|e_i|^{\frac{1}{1+\eta_1}} + d_2 sign(e_i)|e_i|^{\frac{1+2\eta_1}{1+\eta_1}} + d_3 e_i + d_4 sign(e_i)\right)\right) \\
&= \sum_{i=1}^{r} sign(s_i)\left(-D_i + \widehat{D}_i - d_5 sign(s_i)|s_i|^{\frac{1}{1+\eta_2}} - d_6 sign(s_i)|s_i|^{\frac{1+2\eta_2}{1+\eta_2}} - d_7 s_i - d_8 sign(s_i)\right) \\
&\leq \sum_{i=1}^{r} sign(s_i)\left(-d_5 sign(s_i)|s_i|^{\frac{1}{1+\eta_2}} - d_6 sign(s_i)|s_i|^{\frac{1+2\eta_2}{1+\eta_2}} - d_7 s_i\right) \\
&= -d_5\sum_{i=1}^{r}|s_i|^{\frac{1}{1+\eta_2}} - d_6\sum_{i=1}^{r}|s_i|^{\frac{1+2\eta_2}{1+\eta_2}} - d_7\sum_{i=1}^{r}|s_i|
\end{aligned}
$$

$$
\begin{aligned}
&\leq -d_5\left(\sum_{i=1}^{r}|s_i|\right)^{\frac{1}{1+\eta_2}} - d_6 r^{1-(\frac{1+2\eta_2}{1+\eta_2})}\left(\sum_{i=1}^{r}|s_i|\right)^{\frac{1+2\eta_2}{1+\eta_2}} - d_7\left(\sum_{i=1}^{r}|s_i|\right)\\
&= -d_5 V_3^{\frac{1}{1+\eta_2}} - d_6 r^{\frac{-\eta_2}{1+\eta_2}} V_3^{\frac{1+2\eta_2}{1+\eta_2}} - d_7 V_3\\
&= -\frac{\pi(1+\eta_2)}{2\eta_2 T_2} V_3^{\frac{1}{1+\eta_2}} - \frac{\pi(1+\eta_2)}{2\eta_2 T_2 r^{\frac{-\eta_2}{1+\eta_2}}} r^{\frac{-\eta_2}{1+\eta_2}} V_3^{\frac{1+2\eta_2}{1+\eta_2}} - \frac{\pi(1+\eta_2)}{\eta_2 T_2} V_3\\
&= -\frac{\pi(1+\eta_2)}{2\eta_2 T_2}\left(V_3^{\frac{1}{1+\eta_2}} + 2V_3 + V_3^{\frac{1+2\eta_2}{1+\eta_2}}\right)
\end{aligned} \tag{3.20}
$$

Here, we assume that $d_8 > |\tilde{D}_i|$, which satisfies Lemma 2.3. Thus, the error state trajectories will approach the proposed sliding surface in the specified time $T_2$.

**Remark 3.2.** *By combining the results of the theorems, we can conclude that the systems (3.8) and (3.9) achieve synchronization within the predetermined time $T_1 + T_2$.*

## 4. Numerical simulation

The real financial market is usually subject to external interference, and the study of chaos synchronization is helpful to predict the market behavior, prevent the occurrence of financial crisis, and improve the regulatory efficiency. In the simulation, the previously mentioned FO financial system serves as the master system:

$$
\begin{cases}
D^{\rho_1} x_1 = x_3 + (x_2 - a)x_1\\
D^{\rho_2} x_2 = 1 - bx_2 - bx_1^2 - cx_1^6\\
D^{\rho_3} x_3 = -x_1 - dx_3 - ex_1x_2
\end{cases} \tag{4.1}
$$

The slave system is defined as:

$$
\begin{cases}
D^{\rho_1} y_1 = y_3 + (y_2 - a)y_1 + D_1(y,t) + u_1(t)\\
D^{\rho_2} y_2 = 1 - by_2 - by_1^2 - cy_1^6 + D_2(y,t) + u_2(t)\\
D^{\rho_3} y_3 = -y_1 - dy_3 - ey_1y_2 + D_3(y,t) + u_3(t)
\end{cases} \tag{4.2}
$$

Different variables in the financial system often have different characteristics of time memory. For example, the interest rate is greatly affected by long-term economic policies and has strong historical dependence, investment needs to balance historical data with current market conditions, and price indices are more sensitive to short-term fluctuations. Assuming that all variables have the same memory effect may oversimplify these dynamic properties. With the increase of the order, the memory effect of the Caputo derivative weakens [26]. Therefore, $(\rho_1, \rho_2, \rho_3) = (0.97, 0.98, 0.99)$ is chosen as the incommensurate order in order to be more consistent with the characteristics of the actual financial market. Figure 10 illustrates the chaotic behavior of system (4.1) when the orders are $(\rho_1, \rho_2, \rho_3) = (0.97, 0.98, 0.99)$ and the starting states are $(x_1(0), x_2(0), x_3(0)) = (0.4, 0.2, 0.5)$. The initial states of model (4.2) are $(y_1(0), y_2(0), y_3(0)) = (0.5, 3, -0.4)$. The uncertainties are selected as

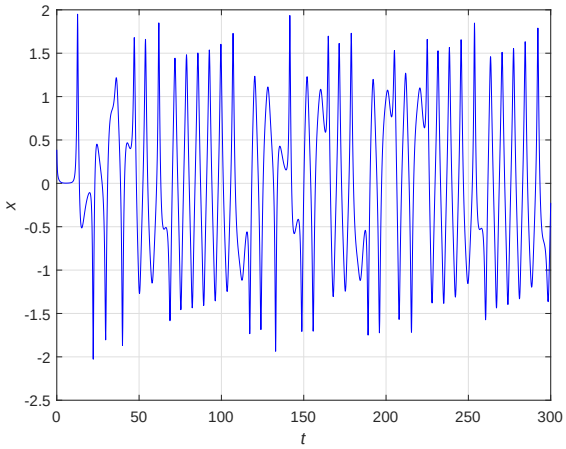


(a) Time history diagram when $(\rho_1, \rho_2, \rho_3) = (0.97, 0.98, 0.99)$

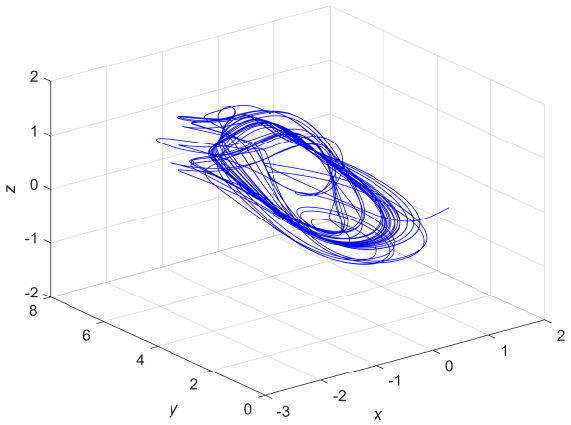


(b) Phase diagram when $(\rho_1, \rho_2, \rho_3) = (0.97, 0.98, 0.99)$

**Figure 10.** Time history and phase diagrams of system (4.1).

$\Delta g_1(y,t) = 2.5cos(6t)y_1$, $\Delta g_2(y,t) = 2cos(2t)y_2$, and $\Delta g_3(y,t) = -2.5sin(3t)y_3$. The external interferences are selected as $d_1(t) = -2sin(t)$, $d_2(t) = 1.5cos(t)$, and $d_3(t) = -sin(6t)$.

In subsequent simulation experiments, we select the number of hidden neurons of the RBFNN as 12, the center value as [–2, –1.5, –1, –0.5, 0, 1, 2, 2.5, 3, 4.5, 5, 6], the width value as 11, the Gaussian radial basis function as activation function, the weight learning rate as 9, the inputs as $y_1, y_2, y_3$, and the approximate effect is shown in Figure 11. As the activation function (2.9) is determined by the center and width values, we analyze how changes in these parameters affect the approximation accuracy. As shown in Figure 12(a), selecting 8 hidden nodes leads to underfitting, which means that the features of the input space cannot be fully expressed. Figure 12(b) shows that increasing the number of hidden nodes to 20 does not significantly enhance approximation performance, indicating a limit to the effectiveness of additional center values. Moreover, the increased computational complexity prolongs the system's synchronization convergence time to 0.2053 s. Similarly, as shown in Figure 13(a), too small a width means that the sensing range of the activation function is limited, reducing approximation effectiveness. Figure 13(b) shows that increasing the width value does not significantly improve approximation performance and prolongs synchronization time to 0.2039 s.

Experiments are implemented to validate the performance of this new approach. The numerical simulations comprise four parts: 1) By changing the system parameters, the performance of the controller when the model parameters are uncertain is studied. 2) By comparing different predefined time and index terms, the influence of different parameters in the controller on the synchronous convergence of the system is studied. 3) By comparing with other SMC schemes, the proposed method's superiority is evaluated. 4) By changing parameters, the robustness of the control method under parameter variation is studied.

### *4.1. The influence of different system parameters*

To evaluate the robustness of the proposed control method under varying system parameters, we conduct a sensitivity analysis by modifying key parameters, including $a, b, c, d, e$. The simulation

results show that, when $T_1 = T_2 = 1$ and $\eta_1 = \eta_2 = 0.5$, despite changes in these parameters, the synchronization convergence time and error curves remain nearly identical, as shown in Figure 14. This demonstrates that the proposed control method is robust to model parameter changes, ensuring system stabilization even under parameter uncertainties. For the subsequent analysis, we fix $a = 4.4, b = 0.1, c = 0.2, d = 0.9, e = 0.06$.

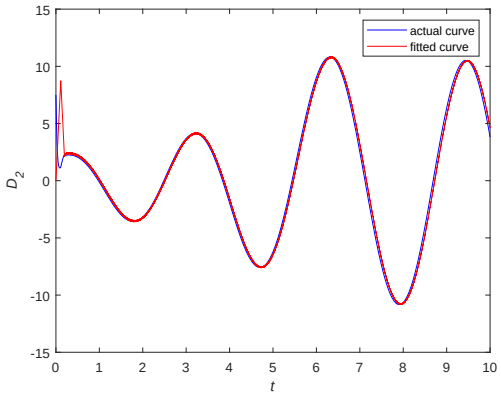


**Figure 11.** Approximation effect when $c_j = [-2, -1.5, -1, -0.5, 0, 1, 2, 2.5, 3, 4.5, 5, 6]$.

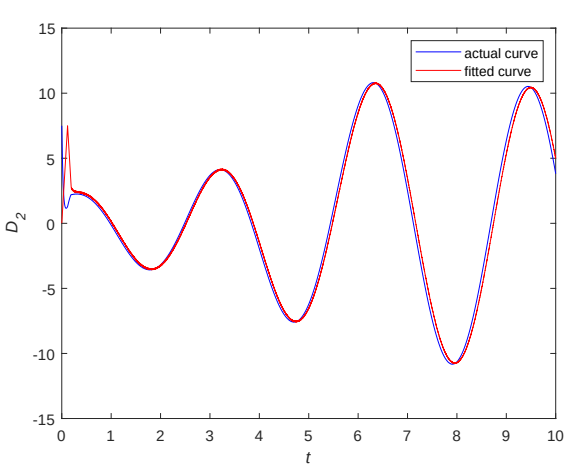


(a) Approximation effect when $c_j = [-2, -1.5, -1, -0.5, 0, 1, 2, 2.5]$

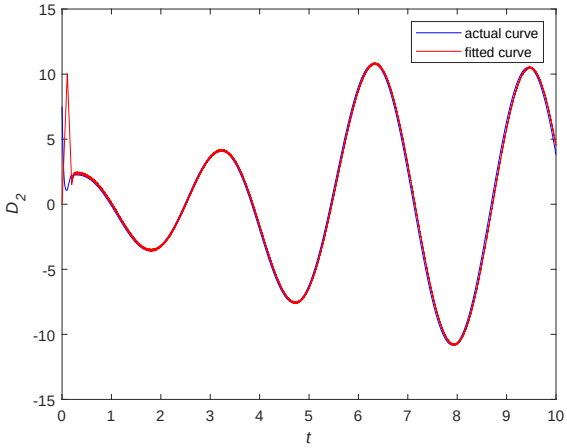


(b) Approximation effect when $c_j = [-7, -6.5, -5.5, -4.5, -3, -2, -1.5, -1, 0, 1, 1.5, 2, 2.5, 3, 4, 5, 5.5, 6, 6.5, 7]$

**Figure 12.** Approximation effect of different center values.

In financial markets, system parameters fluctuate due to shifts in economic policy, market demand, and other macroeconomic factors. Our control method has strong adaptability in different macroeconomic environments, which is particularly important in the case of uncertainty and dynamic changes in financial markets. This feature can be applied to high-frequency trading systems to ensure that trading strategies remain responsive without lagging.

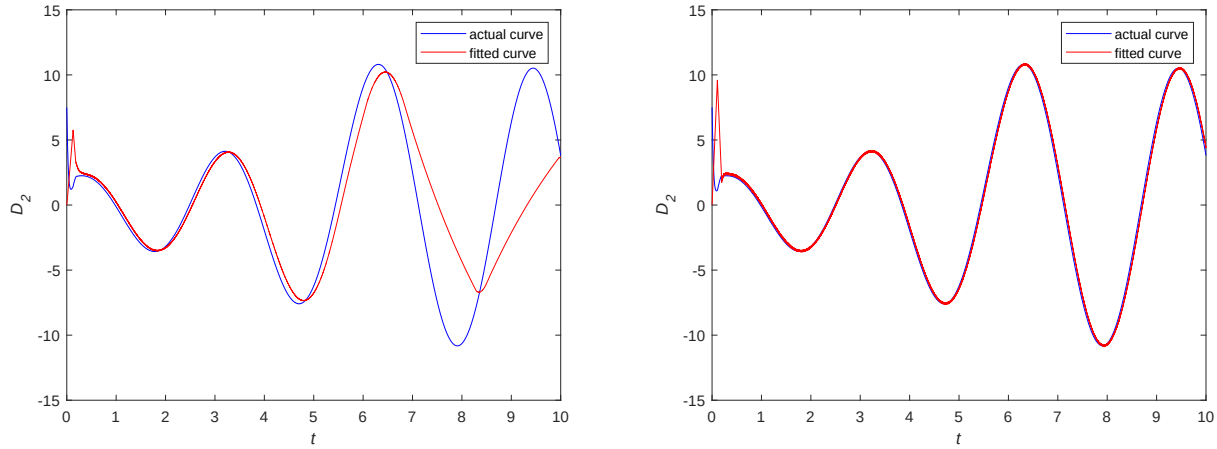


(a) Approximation effect when $b_j = 5$ (b) Approximation effect when $b_j = 15$

**Figure 13.** Approximation effect of different width values.

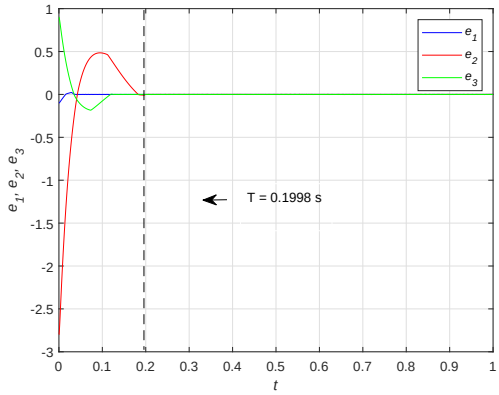


**Figure 14.** Synchronization errors when $T_1 = T_2 = 1$ and $\eta_1 = \eta_2 = 0.5$.

### *4.2. The influence of different controller parameters*

In the controller (3.15), the coefficient $d_i$ is related to $T_i$ and $\eta_i$. $T_1 + T_2$ is the convergence time preset by the user, $\eta_i$ is the exponential term of the controller. It is necessary to study the influence of parameters on the convergence time.

#### 4.2.1. The influence of different predefined time

In this simulation experiment, the predefined time is classified into three cases: (1) $T_1 = T_2 = 0.5$, $T_1 + T_2 = 1$; (2) $T_1 = T_2 = 0.75$, $T_1 + T_2 = 1.5$; (3) $T_1 = T_2 = 1$, $T_1 + T_2 = 2$. Other parameters are set as $\eta_1 = \eta_2 = 0.5$ and $d_4 = d_8 = 2$. Consequently, the calculated values are: (1) $d_1 = d_5 = 3\pi$, $d_2 = d_6 = 3\pi \times 3^{\frac{1}{3}}$, and $d_3 = d_7 = 6\pi$; (2) $d_1 = d_5 = 2\pi$, $d_2 = d_6 = 2\pi \times 3^{\frac{1}{3}}$, and $d_3 = d_7 = 4\pi$; (3) $d_1 = d_5 = 1.5\pi$, $d_2 = d_6 = 1.5\pi \times 3^{\frac{1}{3}}$, and $d_3 = d_7 = 3\pi$. The results are shown in Figure 15. It can be seen that the settling time is reduced compared to the respective predefined time: (1) 0.1154 s < 1 s; (2) 0.1553 s < 1.5 s; (3) 0.1998 s < 2 s. Since case (3) has been shown in Figure 14, it will not be repeated

here. From 0.1154 s < 0.1553 s < 0.1998 s, we can conclude that the larger the predefined time, the slower the convergence speed. So the users can flexibly adjust the predefined time as required.

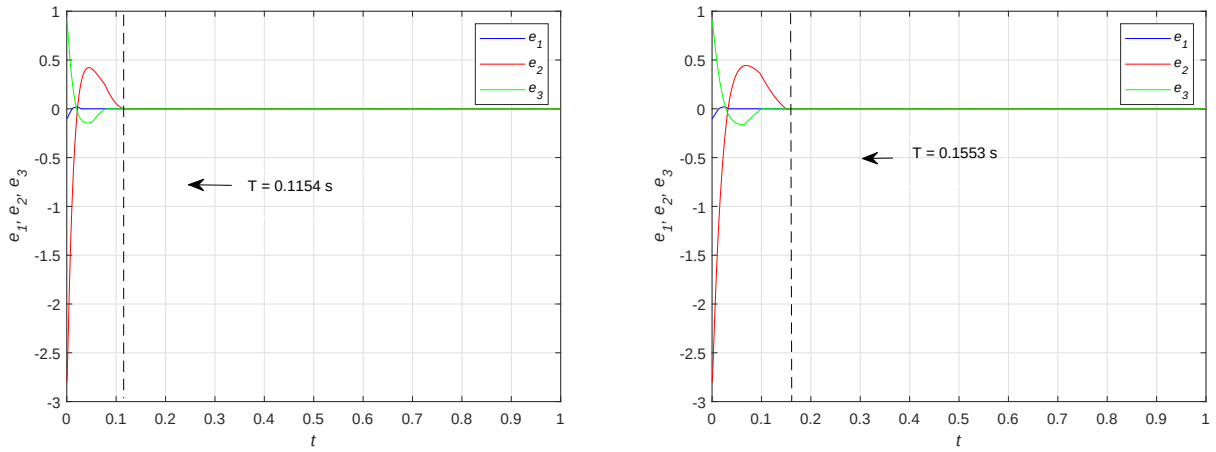


(a) Synchronization errors when $T_1 = T_2 = 0.5$ (b) Synchronization errors when $T_1 = T_2 = 0.75$

**Figure 15.** Synchronization errors with different predefined times.

### 4.2.2. The influence of different $\eta_i$

In this simulation experiment, $\eta_i$ is classified into three cases: (1) $\eta_1 = \eta_2 = \frac{1}{3}$; (2) $\eta_1 = \eta_2 = 0.5$; (3) $\eta_1 = \eta_2 = \frac{2}{3}$. Other parameters are set as $T_1 = T_2 = 1$ and $d_4 = d_8 = 2$. Consequently, the calculated values are: (1) $d_1 = d_5 = 2\pi$, $d_2 = d_6 = 2\pi \times 3^{\frac{1}{4}}$, and $d_3 = d_7 = 4\pi$; (2) $d_1 = d_5 = 1.5\pi$, $d_2 = d_6 = 1.5\pi \times 3^{\frac{1}{3}}$, and $d_3 = d_7 = 3\pi$; (3) $d_1 = d_5 = \frac{5}{4}\pi$, $d_2 = d_6 = \frac{5}{4}\pi \times 3^{\frac{2}{5}}$, and $d_3 = d_7 = \frac{5}{2}\pi$. The results are shown in Figure 16. It is observed that the settling times are: (1) 0.1616 s; (2) 0.1998 s; (3) 0.2254 s. Since case (2) has been shown in Figure 14, it will not be repeated here. From 0.1616 s < 0.1998 s < 0.2254 s, we can conclude that the larger the exponential term, the faster the convergence speed. So the users can flexibly adjust the $\eta_i$ as required.

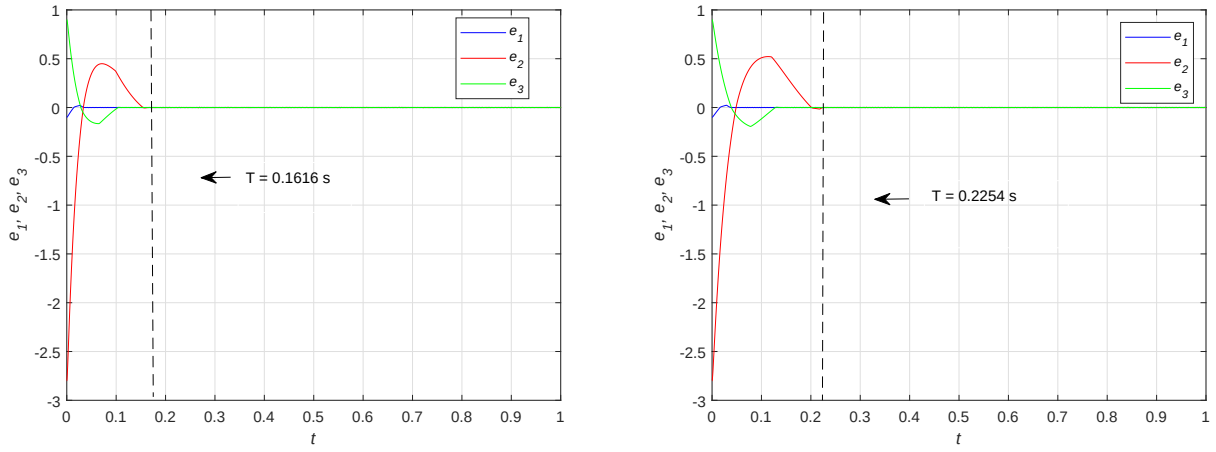


(a) Synchronization errors when $\eta_1 = \eta_2 = \frac{1}{3}$ (b) Synchronization errors when $\eta_1 = \eta_2 = \frac{2}{3}$

**Figure 16.** Synchronization errors with different exponential terms.

The simulation results show that the controller parameters significantly influence the synchronous convergence time. In financial markets, this implies that market participants can adjust the predefined time based on market conditions to regulate the reaction rate. In volatile markets, selecting a shorter predefined time allows the system to adapt more quickly to market changes, reducing potential losses. In stable markets, choosing a longer predefined time ensures smoother system operation, preventing excessive intervention.

In subsequent comparative simulations, we fix $T_1 = T_2 = 1$ and $\eta_1 = \eta_2 = 0.5$.

### *4.3. Comparative simulations*

#### 4.3.1. Comparison of the predefined-time SMC methods with and without the RBFNN

For convenience, many studies estimate the upper bounds of uncertainties and perturbations. In real life, uncertainties and perturbations are difficult to estimate accurately, and conservative estimations often result in large control inputs, leading to unnecessary wastage. To illustrate the superiority of the RBFNN estimator, we compare the two methods: the sliding surface (3.11) is used as described above, while the controller is defined as follows:

$$\begin{aligned} u_i = f_i - g_i + D^{\rho-1}\left(d_1 sign\left(e_i\right)|e_i|^{\frac{1}{1+\eta_1}} + d_2 sign\left(e_i\right)|e_i|^{\frac{1+2\eta_1}{1+\eta_1}} + d_3 e_i + d_4 sign\left(e_i\right)\right) \\ + d_5 sign\left(s_i\right)|s_i|^{\frac{1}{1+\eta_2}} + d_6 sign\left(s_i\right)|s_i|^{\frac{1+2\eta_2}{1+\eta_2}} + d_7 s_i + d_8 sign\left(s_i\right) + \left(\beta_i |y_i| + D^s\right) sign\left(s_i\right) \end{aligned} \tag{4.3}$$

where $\beta_i$, $D^s$ are the boundaries of instabilities and fluctuations, $|\Delta g_i(\boldsymbol{y}, t)| \leq \beta_i |y_i|$, $|d_i(t)| \leq D^s$. The other parameters are the same as the preceding values. The experimental results are displayed in Figure 17. Figure 17(a) illustrates that $e_1, e_2, e_3$ converge to zero within 0.2024 s under controller (4.3), and Figures 17(b)–(d) show the control inputs for both methods. It is clear that the input amplitude of controller (4.3) is larger than that of controller (3.15).

Obviously, the control approach suggested in this work not only guarantees the convergence time but also reduces the error buffeting and control input. In actual financial market interventions, the control input can be regarded as the strength of the macro-control. Regulators usually want to maintain financial stability with minimal policy intervention, avoiding market imbalances or waste of resources. Traditional control methods rely on large control inputs to achieve rapid convergence, but this may lead to irrational market fluctuations, the rise of policy costs, and even foster "policy dependence". In contrast, our approach ensures synchronization while reducing control inputs to achieve the same market stability effect, thereby improving regulatory efficiency. In addition, because the RBFNN can adaptively adjust the level of intervention, our approach can be adapted to different market environments. Therefore, this control strategy can better cope with market disturbances, and can be used in a financial supervision system. The following analyses will focus on controllers utilizing the RBFNN.

#### 4.3.2. Comparison of various stabilization time methods with the RBFNN

To emphasize the benefits of this predetermined-time method, this part discusses the findings of different stabilization methods. In the finite-time SMC method, the sliding surface and controller are employed as follows:

$$s_i = D^{\rho-1} e_i + D^{\rho-2}\left(a_1 sign\left(e_i\right)|e_i|^{\eta_1} + a_2 sign\left(e_i\right)\right) \tag{4.4}$$

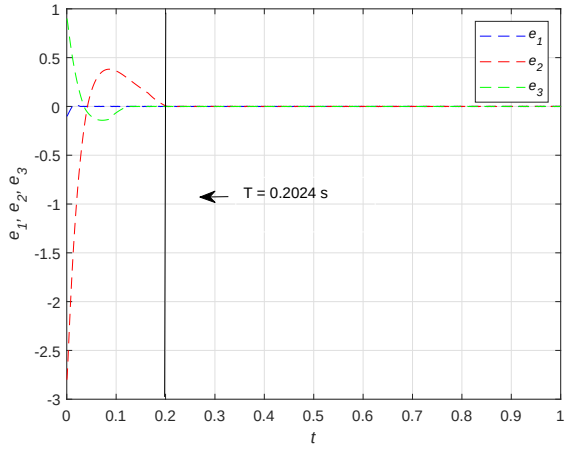


(a) Synchronization errors of the predefined-time control scheme without the RBFNN

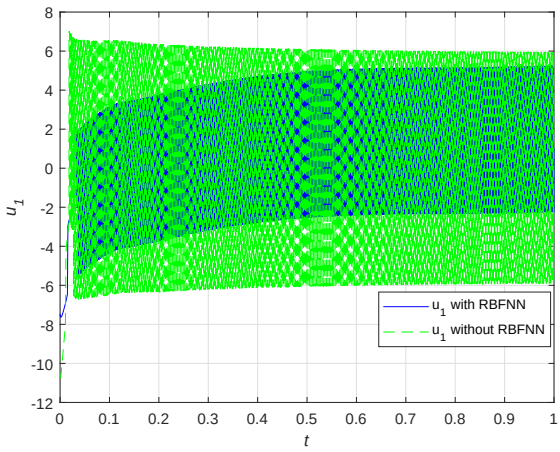


(b) Control input $u_1$ of two predefined-time control schemes

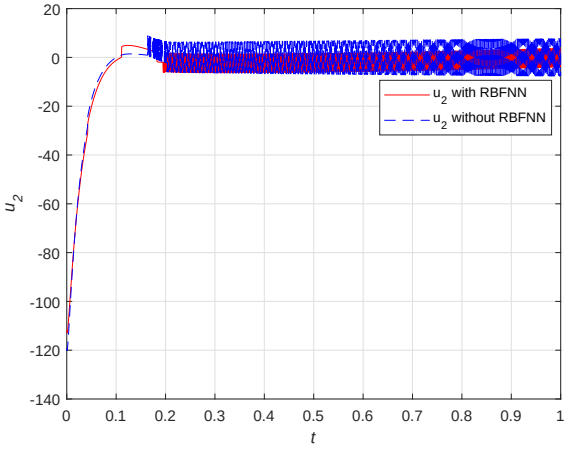


(c) Control input $u_2$ of two predefined-time control schemes

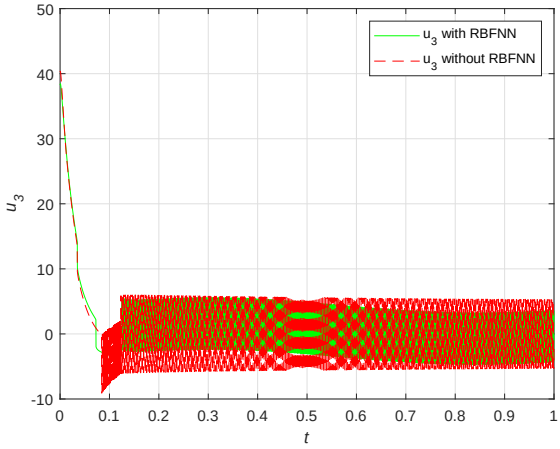


(d) Control input $u_3$ of two predefined-time control schemes

**Figure 17.** Synchronization behaviors of two predefined-time control schemes.

$$u_i = f_i - g_i - \widehat{D}_i + D^{\rho-1}\left(a_1 sign\left(e_i\right)|e_i|^{\eta_1} + a_2 sign\left(e_i\right)\right) + a_3 sign\left(s_i\right)|s_i|^{\eta_2} + a_4 sign\left(s_i\right) \tag{4.5}$$

where $a_1 = a_3 = 1.5\pi$, $a_2 = a_4 = 2$, $\eta_1 = \eta_2 = \frac{2}{3}$. Figure 18(a) illustrates that $e_1, e_2, e_3$ converge to zero within 0.5924 s. Moreover, in the fixed-time SMC method, we use the following sliding-mode surface and controller:

$$s_i = D^{\rho-1}e_i + D^{\rho-2}\left(b_1 sign\left(e_i\right)|e_i|^{\eta_1} + b_2 sign\left(e_i\right)|e_i|^{\eta_3} + b_3 sign\left(e_i\right)\right) \tag{4.6}$$

$$\begin{aligned} u_i = {} & f_i - g_i - \widehat{D}_i + D^{\rho-1}\left(b_1 sign\left(e_i\right)|e_i|^{\eta_1} + b_2 sign\left(e_i\right)|e_i|^{\eta_3} + b_3 sign\left(e_i\right)\right) + b_4 sign\left(s_i\right)|s_i|^{\eta_2} \\ & + b_5 sign\left(s_i\right)|s_i|^{\eta_4} + b_6 sign\left(s_i\right) \end{aligned} \tag{4.7}$$

where $b_1 = b_4 = 1.5\pi$, $b_2 = b_5 = 1.5\pi \times 3^{\frac{1}{3}}$, $b_3 = b_6 = 2$, $\eta_1 = \eta_2 = \frac{2}{3}$, $\eta_3 = \eta_4 = \frac{4}{3}$. Figure 18(b) illustrates that $e_1, e_2, e_3$ will converge to zero within 0.3126 s.

In addition, we also compare it with the method proposed in [40], where the sliding mode surface and controller are presented below:

$$s_i = D^{\rho-1}e_i + D^{\rho-2}\left(c_1 sign\,(e_i)\,|e_i|^{\frac{1+\eta_1}{2}} + c_2 sign\,(s_i)\,|e_i|^{\frac{3-\eta_1}{2}} + c_3 e_i + c_4 sign\,(e_i)\right) \tag{4.8}$$

$$\begin{aligned} u_i = {} & f_i - g_i - \widehat{D}_i + D^{\rho-1}\left(c_1 sign\,(e_i)\,|e_i|^{\frac{1+\eta_1}{2}} + c_2 sign\,(s_i)\,|e_i|^{\frac{3-\eta_1}{2}} + c_3 e_i + +c_4 sign\,(e_i)\right) \\ & + c_5 sign\,(s_i)\,|s_i|^{\frac{1+\eta_2}{2}} + c_6 sign\,(s_i)\,|s_i|^{\frac{3-\eta_2}{2}} + c_7 s_i + c_8 sign\,(s_i) \end{aligned} \tag{4.9}$$

where $c_1 = c_5 = 3$, $c_2 = c_6 = 3^{\frac{4}{3}}$, $c_3 = c_7 = 6$, $c_4 = c_8 = 2$, $\eta_1 = \eta_2 = \frac{1}{3}$, $T_1 = T_2 = 1$. Figure 18(c) illustrates that $e_1, e_2, e_3$ will converge to zero within 0.2860 s.

The simulation results show that the proposed control method converges faster than finite time, fixed time, and other predefined-time SMC methods. This feature is particularly important in high-frequency trading and real-time risk management. The rapid volatility of the financial market requires that the trading system and regulatory mechanism can respond quickly. Faster convergence means traders can adjust their strategies more timely, while regulators can identify market anomalies more swiftly, thereby improving regulatory efficiency and reducing systemic risks.

### *4.4. Robustness analysis*

In this part of the simulation experiment, we discuss the convergence time of each method under different parameters to strengthen the comparative analysis, and because the model (3.7) exhibits two chaotic states, it is crucial to analyze the influence of different sets of incommensurate orders on synchronous convergence. The starting conditions and the values of the uncertainties remain consistent with the previous content. The detailed analysis process will not be reiterated here. Figure 19 illustrates the chaotic behavior of model (4.1) when the orders are $(\rho_1, \rho_2, \rho_3) = (0.79, 0.8, 0.81)$. For the sake of analysis, we let $T_1 = T_2$, $\eta_1 = \eta_2$, and $d_4 = d_8$. Table 2 presents the convergence times of SMC methods with different parameters values. 1) is the finite-time SMC method; 2) is the fixed-time SMC method; 3) is the predefined-time SMC method in [40]; 4) is the predefined-time SMC method without the RBFNN; 5) is the introduced predefined-time SMC method with the RBFNN.

**Remark 4.1.** *From Table 2, it can be concluded that different parameter values have little effect on the synchronization performance of the introduced method, and the proposed predefined-time scheme demonstrates a faster convergence time compared to other schemes.*

## 5. Application

Wu et al. [56] demonstrated that FO chaotic encryption further enlarges the key space compared to integer-order chaotic encryption, and FO chaotic mapping only has short memory effects. Based on these advantages, this paper employs the FO chaotic systems (4.1) and (4.2) for the encryption of images, voice, and signals.

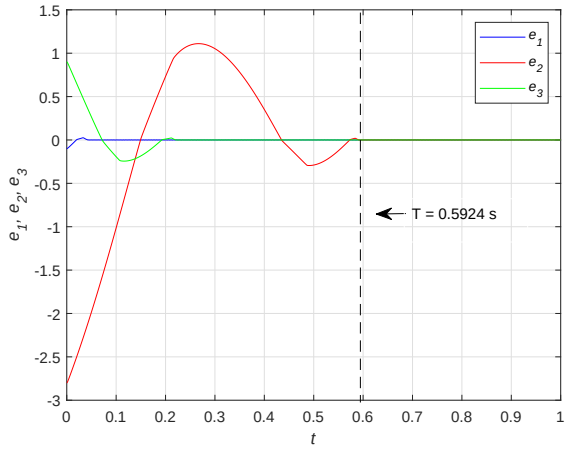


(a) Synchronization errors in the finite-time control scheme

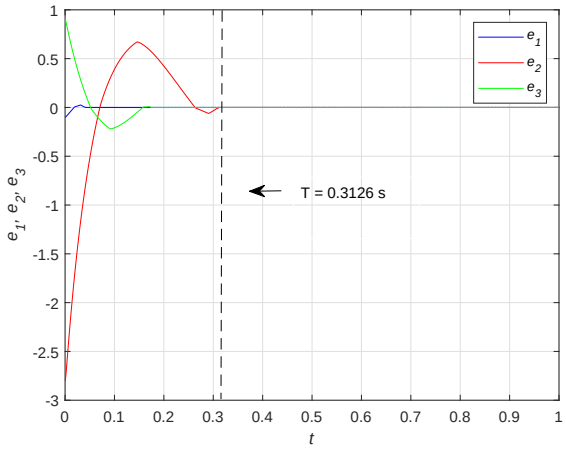


(b) Synchronization errors in the fixed-time control scheme

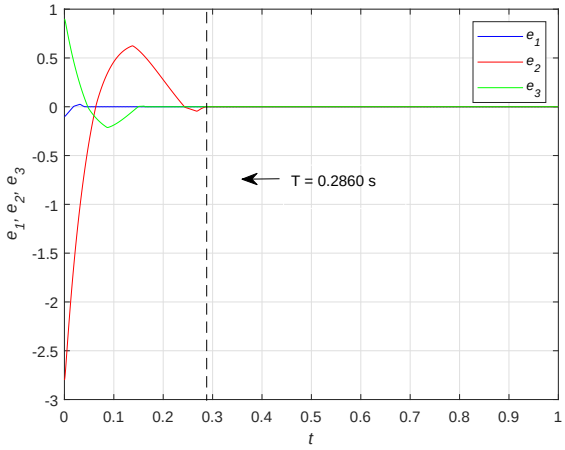


(c) Synchronization errors of the predefined-time control scheme in [40]

**Figure 18.** Synchronization errors in different control schemes.

### *5.1. Chaotic encryption*

To verify the encryption effect of the system (4.1), we apply its chaotic sequences to both image encryption and voice encryption. The chaotic sequences are generated for two sets of fractional orders: $(\rho_1, \rho_2, \rho_3) = (0.97, 0.98, 0.99)$ and $(\rho_1, \rho_2, \rho_3) = (0.79, 0.8, 0.81)$, respectively.

#### 5.1.1. Image encryption

For image encryption, a color image is selected as the original input, which is then divided into small blocks. These blocks are encoded and processed using chaotic sequences combined with DNA coding rules. Finally, the encrypted image is obtained by recombining the processed blocks. Figure 20 shows the original and the encrypted images. Clearly, the encrypted image lacks recognizable characteristics of the original image, indicating that chaotic encryption ensures the security of the plaintext image during communication.

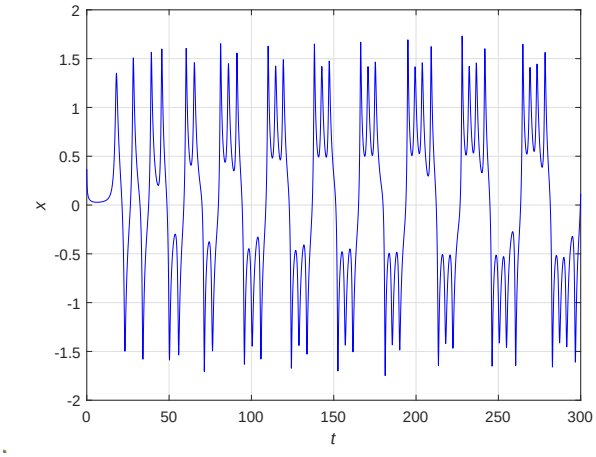


(a) Time history diagram when $(\rho_1, \rho_2, \rho_3) = (0.79, 0.8, 0.81)$

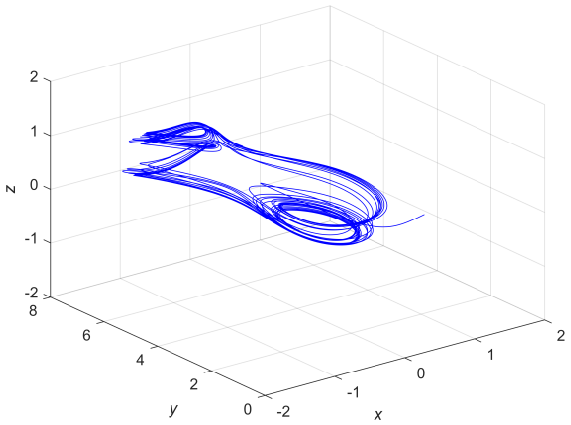


(b) Phase diagram when $(\rho_1, \rho_2, \rho_3) = (0.79, 0.8, 0.81)$

**Figure 19.** Time history and phase diagrams of system (4.1).

**Table 2.** Convergence time of SMC methods with different parameter values.

| Fixed parameter values | Variable parameter values | (1) | (2) | (3) | (4) | (5) |
|---|---|---|---|---|---|---|
| $\eta_1 = 0.5, d_4 = 2$ | $T_1 = 0.5$ | 0.3513 | 0.1787 | 0.1619 | 0.1211 | 0.1154 |
| | $T_1 = 0.75$ | 0.4747 | 0.2534 | 0.1869 | 0.1651 | 0.1553 |
| | $T_1 = 1$ | 0.5924 | 0.3126 | 0.2860 | 0.2020 | 0.1998 |
| $T_1 = 1, d_4 = 2$ | $\eta_1 = \frac{1}{3}$ | 0.4825 | 0.2706 | 0.2390 | 0.1698 | 0.1616 |
| | $\eta_1 = 0.5$ | 0.5924 | 0.3126 | 0.2860 | 0.2020 | 0.1998 |
| | $\eta_1 = \frac{2}{3}$ | 0.6737 | 0.3422 | 0.3180 | 0.2257 | 0.2254 |
| $T_1 = 1, \eta_1 = 0.5$ | $d_4 = 1$ | 0.7848 | 0.3955 | 0.3570 | 0.2681 | 0.2447 |
| | $d_4 = 2$ | 0.5924 | 0.3126 | 0.2860 | 0.2020 | 0.1998 |
| | $d_4 = 3$ | 0.4855 | 0.2668 | 0.2430 | 0.1796 | 0.1657 |
| $T_1 = 1, \eta_1 = 0.5, d_4 = 2$ | $\boldsymbol{\rho} = (0.79, 0.8, 0.81)$ | 0.5477 | 0.3238 | 0.2975 | 0.2155 | 0.2153 |

To access the security of image encryption performance, three indicators, histogram, adjacent pixel correlation, and information entropy, are analyzed in this part.

1) Histogram

The histogram reflects the pixel distribution of the image and is the key index of security evaluation. Figures 21 and 22 show the histograms of the R, G, and B components for the original and encrypted images, respectively. Figure 22 shows that the pixel distribution of the encrypted image is uniform, eliminating the distinguishing feature of the pixel distribution of the original image.

2) Image adjacent pixel correlation

The correlation coefficient is a key metric for assessing the robustness of the encryption algorithm against statistical analysis attacks. The following formulas are used to compute the correlation coefficients [57]:

(a) The original image (b) The encrypted image

**Figure 20.** The results of image encryption.

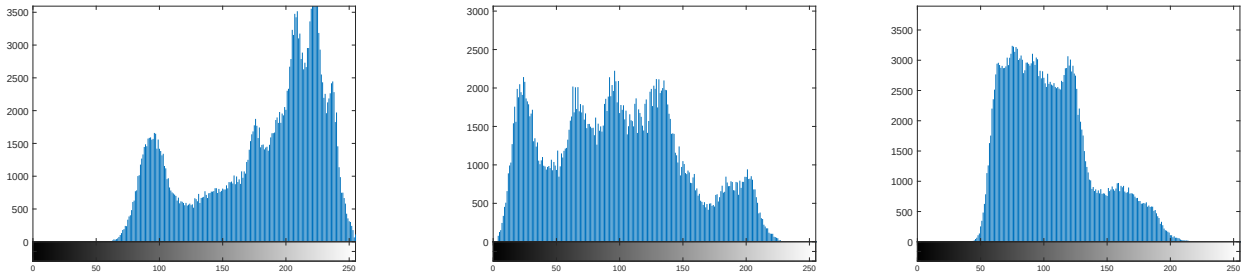

(a) The histogram of the red component (b) The histogram of the green component (c) The histogram of the blue component

**Figure 21.** The histograms of the original image.

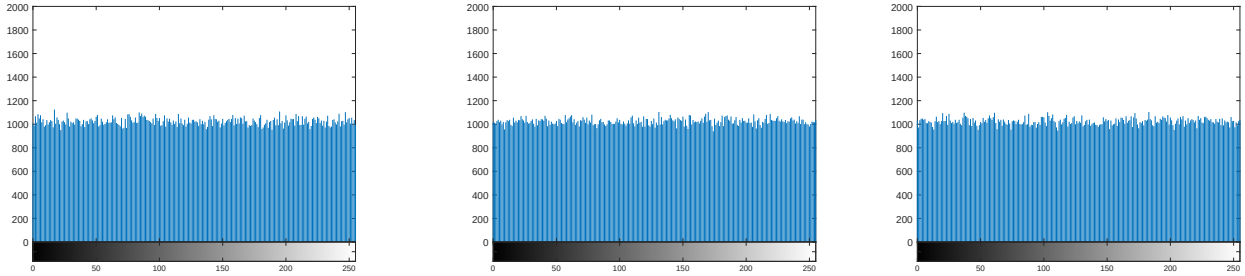

(a) The histogram of the red component (b) The histogram of the green component (c) The histogram of the blue component

**Figure 22.** The histograms of the encrypted image.

$$E(X) = \frac{1}{N}\sum_{p=1}^{N} X_p \tag{5.1}$$

$$D(X) = \frac{1}{N}\sum_{p=1}^{N}\left(X_p - E(X)\right)^2 \tag{5.2}$$

$$\mathrm{cov}(X, Y) = \frac{1}{N}\sum_{p=1}^{N}(X_p - E(X))(Y_p - E(Y)) \tag{5.3}$$

$$r_{XY} = \frac{\mathrm{cot}(X, Y)}{\sqrt{D(X)} \times \sqrt{D(Y)}} \tag{5.4}$$

where $X$ and $Y$ are adjacent pixels, $E(X)$ and $E(Y)$ are the mathematical expectation, $D(X)$ is the variance, $cov(X, Y)$ is the covariance, $r_{XY}$ is the correlation coefficient, $N$ is the set of randomly sampled pixels, and here, $N$ is 5000. Tables 3 and 4 show the correlation coefficients $r_{XY}$ of the three components in three directions: horizontal, vertical, and diagonal. As shown in the tables, the correlation coefficient $r_{XY}$ of the original image is close to 1, while the correlation coefficient $r_{XY}$ of the encrypted image is close to 0. This indicates that the encryption algorithm has diffusion characteristics.

**Table 3.** The correlation coefficients of the three components of the original image.

| Original image | Horizontal | Vertical | Diagonal |
|---|---|---|---|
| R | 0.9805 | 0.9899 | 0.9710 |
| G | 0.9712 | 0.9835 | 0.9564 |
| B | 0.9387 | 0.9596 | 0.9199 |

**Table 4.** The correlation coefficients of the three components of the encrypted image.

| Encrypted image | Horizontal | Vertical | Diagonal |
|---|---|---|---|
| R | 0.0032 | 0.0119 | 0.0269 |
| G | 0.0161 | -0.0048 | 0.0028 |
| B | 0.0045 | -0.0195 | -0.0075 |

3) Information entropy

The increase of information entropy $H$ indicates that the uncertainty in the image is enhanced, while the decrease indicates that the image is regular. The following formula is used to compute information entropy:

$$H = -\sum_{j=1}^{L} P(j)\log_2 P(j) \tag{5.5}$$

where $L$ is the gray level of the image and $P(j)$ is the probability of the occurrence of $j$. Table 5 shows the entropy $H$ of the three channels. A value of $H$ approaching 8 means that the image exhibits greater randomness. As shown in the table, the encrypted image's entropy $H$ is closer to 8, which indicates that the encryption algorithm enhances the randomness of the original image. From the above analysis, the image encryption is successful.

**Table 5.** The information entropy of the original and encrypted images.

| Image | R | G | B |
|---|---|---|---|
| Original image | 7.2531 | 7.5952 | 6.9686 |
| Encrypted image | 7.9993 | 7.9993 | 7.9993 |

### 5.1.2. Voice encryption

For voice encryption, nonlinear transformations are applied to the chaotic sequences, followed by multiple XOR operations for encryption. Figure 23 illustrates the waveform diagrams of both the original and encrypted voices. It can be seen that the encrypted voice and the original voice are completely different in the time domain, which indicates that the voice encryption is successful.

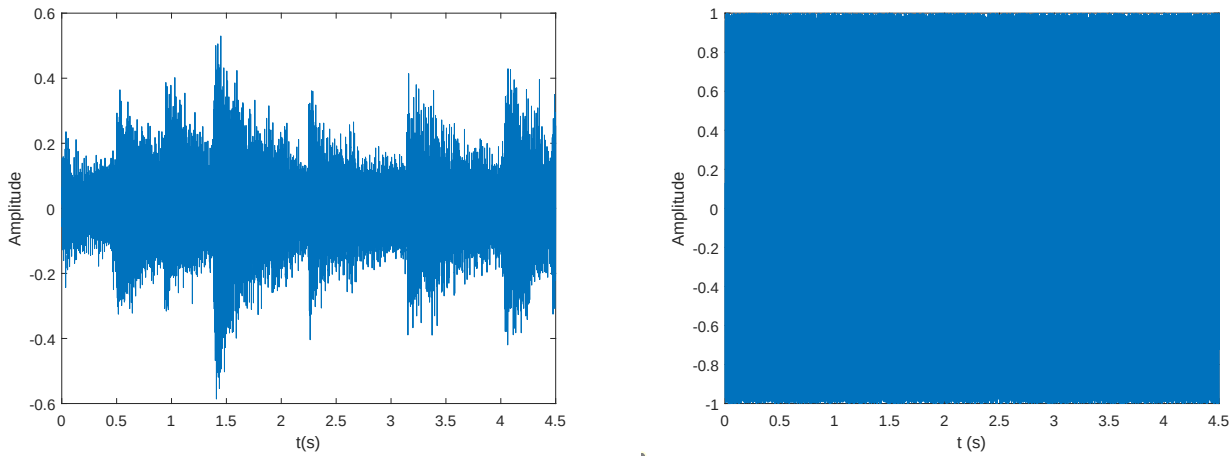


(a) The original voice (b) The encrypted voice

**Figure 23.** The results of voice encryption.

To evaluate the security of voice encryption performance, spectrum analysis, correlation analysis, and information entropy analysis are discussed in this part. Correlation analysis and information entropy analysis are similar to the above processes and will not be repeated here.

1) Voice spectrum

Figure 24 shows the spectrum diagrams, where the encrypted voice spectrum has no obvious peak value and shows a uniform distribution, indicating a significant difference from the original voice. These results verify the performance of the encryption method.

2) Voice adjacent sample correlation

As shown in Table 6, the original voice's $r_{XY}$ is close to 1, while the encrypted voice's $r_{XY}$ is close to 0, which indicates that the encryption algorithm has diffusion characteristics.

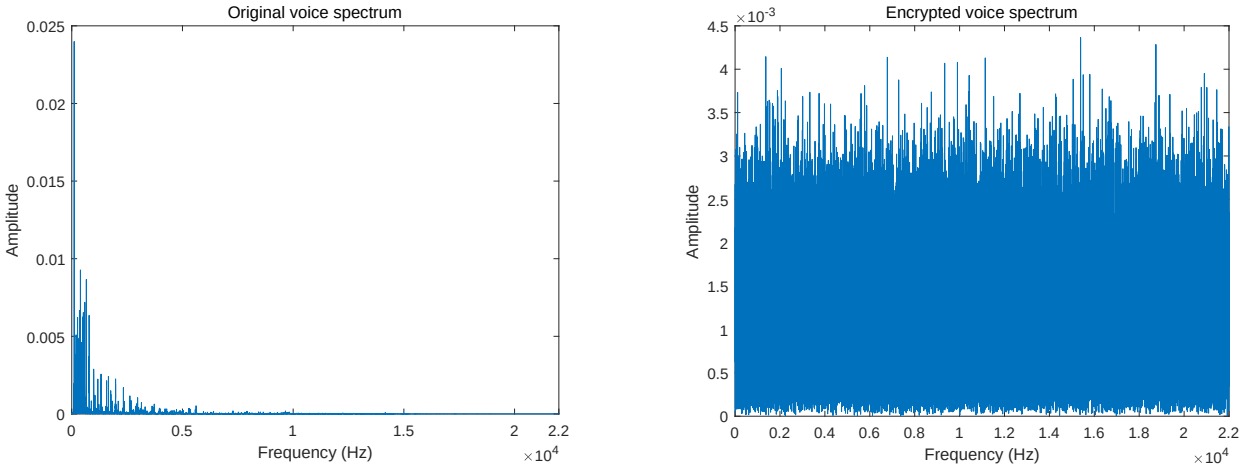


(a) The spectrum of the original voice

(b) The spectrum of the encrypted voice

**Figure 24.** The voice spectrum.

3) Information entropy

As shown in Table 6, the encrypted voice's $H$ is closer to 8, which indicates that the encryption algorithm enhances the randomness of the original voice.

**Table 6.** The correlation coefficient and information entropy of the original and encrypted voice.

| Analysis | Original voice | Encrypted voice |
|---|---|---|
| Correlation | 0.9926 | -0.0027 |
| Entropy | 6.6270 | 7.9990 |

### *5.2. Chaos masking*

Chaos masking is an encrypted communication method that uses chaotic signals to hide useful signals. Its schematic diagram is shown in Figure 25. At the sending end, the useful signal $S(t)$ is superimposed with the chaotic sequence generated by the drive model (4.1) to obtain the encrypted signal $S_e(t)$. $S_e(t)$ is then transmitted to the receiving end, where the synchronization is realized using the predefined-time SMC strategy. The chaotic sequence generated by the response model (4.2) is selected for decryption, resulting in the decrypted signal $S_d(t)$. In this part, the master-slave models described in Section 4, along with the suggested predefined-time SMC approach, are used for chaotic masking. The fractional orders are set to $(\rho_1, \rho_2, \rho_3) = (0.97, 0.98, 0.99)$, the system's initial values, predefined times, control parameters, and other settings remain consistent with those in Section 4. The useful signal is chosen as $S(t) = sin(3t - 3)cos(t)$. Figure 26 indicates the three signals and it is found that $S_e(t)$ is different with $S(t)$, while $S_d(t)$ is consistent with $S(t)$. The findings reveal that the introduced control approach can effectively realize secure communication. When the orders are set to $(\rho_1, \rho_2, \rho_3) = (0.79, 0.8, 0.81)$, the analysis process is consistent with the aforementioned discussion. Therefore, further details are omitted here for brevity.

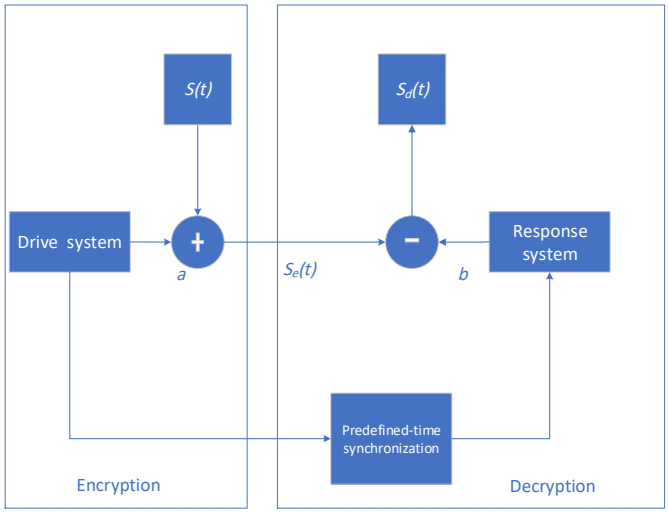


**Figure 25.** The process diagram of chaotic masking [58].

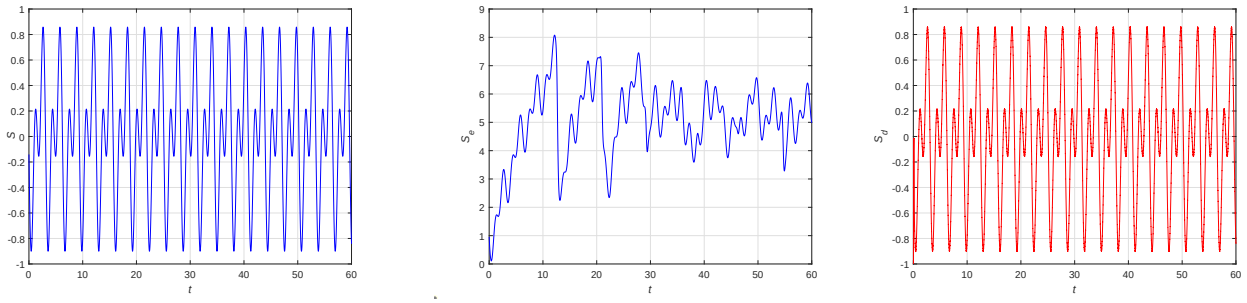

(a) The useful signal (b) The encrypted signal (c) The decrypted signal

**Figure 26.** The results of chaotic masking.

The simulation results of chaos encryption and chaos masking demonstrate that the proposed system and control method have significant practical value in financial market data security. The financial market relies on high-speed data transmission and secure communication. The chaotic encryption method can safeguard trading orders, market data, and financial communications from theft or tampering during transmission. Financial institutions and regulators can use this method to protect high-frequency trading orders, bank payment information, and regulatory report data. This ensures the integrity and confidentiality of information during transmission, reducing potential security risks.

## 6. Conclusions

In this work, we present an innovative FO financial chaotic system considering the non-constant elasticity of demand and the memory effect of financial variables. The dynamic behaviors of the model are explored using bifurcation diagrams, LE diagrams, time history diagrams, phase diagrams, a 0-1 test, and a Poincaré map. To address the synchronization challenges of chaotic models with instabili-

ties and external perturbations, we use an RBFNN to estimate nonlinear functions. Based on Lyapunov stability theory, we develop an innovative predefined-time SMC method incorporating an RBFNN to achieve fast synchronization of FO financial systems. Simulation findings reveal that the approach features the benefits of short synchronization time, predefinable control parameters, and small control input. Furthermore, chaotic encryption and chaos masking are implemented using chaotic systems and synchronization methods to ensure secure information transmission. The proposed FO financial chaos system provides new insights into economic modeling and captures the complex dynamics of financial markets more accurately. The robust control method developed ensures the stability of chaotic systems with uncertain parameters and external interference, contributing to the development of nonlinear control theory. Furthermore, the chaotic encryption technique demonstrates great promise in securing financial data transmission and enhancing communication security. In future studies, optimizing RBFNN parameters using advanced algorithms such as reinforcement learning or evolutionary strategies may further improve synchronization performance. Additionally, exploring more complex fractional financial models with real-world data validation can improve practical applicability. Beyond the financial field, the control scheme is universal and can be extended to other engineering areas such as event-triggered control, autonomous underwater vehicle (AUV) path tracking, and power system stability control.

## Use of AI tools declaration

The authors declare they have not used Artificial Intelligence (AI) tools in the creation of this article.

## Conflict of interest

The authors declare there are no conflicts of interest.

## References

1. I. Podlubny, *Fractional Differential Equations*, Academic Press, 1999.
2. J. M. Munoz-Pacheco, E. Zambrano-Serrano, C. Volos, O. I. Tacha, I. N. Stouboulos, V. T. Pham, A fractional order chaotic system with a 3D grid of variable attractors, *Chaos Solitons Fractals*, **113** (2018), 69–78. https://doi.org/10.1016/j.chaos.2018.05.015
3. P. Ostalczyk, *Discrete Fractional Calculus: Applications in Control and Image Processing*, World Scientific, 2016. https://doi.org/10.1142/9833
4. L. C. de Barros, M. M. Lopes, F. S. Pedro, E. Esmi, J. P. C. dos Santos, D. E. Sánchez, The memory effect on fractional calculus: an application in the spread of COVID-19, *Comput. Appl. Math.*, **40** (2021), 72. https://doi.org/10.1007/s40314-021-01456-z
5. S. B. Chen, H. Jahanshahi, O. A. Abba, J. E. Solís-Pérez, S. Bekiros, J. F. Gómez-Aguilar, et al., The effect of market confidence on a financial system from the perspective of fractional calculus: Numerical investigation and circuit realization, *Chaos Solitons Fractals*, **140** (2020), 110223. https://doi.org/10.1016/j.chaos.2020.110223

6. H. Jahanshahi, A. Yousefpour, J. M. Munoz-Pacheco, S. Kacar, V. T. Pham, F. E. Alsaadi, A new fractional-order hyperchaotic memristor oscillator: Dynamic analysis, robust adaptive synchronization, and its application to voice encryption, *Appl. Math. Comput.*, **383** (2020), 125310. https://doi.org/10.1016/j.amc.2020.125310
7. S. Vaidyanathan, C. Volos, *Advances and Applications in Chaotic Systems*, Springer, 2016. https://doi.org/10.1007/978-3-319-30279-9
8. R. H. Strotz, J. C. McAnulty, J. B. Naines, Goodwin's nonlinear theory of the business cycle: an electro-analog solution, *Econometrica, J. Econometric Soc.*, **21** (1953), 390–411. https://doi.org/10.2307/1905446
9. J. H. Ma, Y. S. Chen, Study for the bifurcation topological structure and the global complicated character of a kind of nonlinear finance system (I), *Appl. Math. Mech.*, **22** (2001), 1240–1251. https://doi.org/10.1007/bf02437847
10. J. H. Ma, Y. S. Chen, Study for the bifurcation topological structure and the global complicated character of a kind of nonlinear finance system (II), *Appl. Math. Mech.*, **22** (2001), 1375–1382. https://doi.org/10.1007/bf02435540
11. Q. Gao, J. H. Ma, Chaos and Hopf bifurcation of a finance system, *Nonlinear Dyn.*, **58** (2009), 209–216. https://doi.org/10.1007/s11071-009-9472-5
12. O. I. Tacha, C. K. Volos, I. N. Stouboulos, I. M. Kyprianidis, Analysis, adaptive control and circuit simulation of a novel finance system with dissaving, *Arch. Control Sci.*, **26** (2016), 95–115. https://doi.org/10.1515/acsc-2016-0006
13. S. Vaidyanathan, C. K. Volos, O. I. Tacha, I. M. Kyprianidis, I. N. Stouboulos, V. T. Pham, Analysis, control and circuit simulation of a novel 3-D finance chaotic system, in *Advances and Applications in Chaotic Systems*, Springer, (2016), 495–512. https://doi.org/10.1007/978-3-319-30279-9_21
14. S. Vaidyanathan, A. Sambas, S. Kacar, U. Cavusoglu, A new finance chaotic system, its electronic circuit realization, passivity based synchronization and an application to voice encryption, *Nonlinear Eng.*, **8** (2019), 193–205. https://doi.org/10.1515/nleng-2018-0012
15. T. Yang, Dynamical analysis on a finance system with nonconstant elasticity of demand, *Int. J. Bifurcation Chaos*, **30** (2020), 2050148. https://doi.org/10.1142/s0218127420501485
16. B. Subartini, S. Vaidyanathan, A. Sambas, Multistability in the finance chaotic system, its bifurcation analysis and global chaos synchronization via integral sliding mode control, *IAENG Int. J. Appl. Math.*, **51** (2021), 995–1002.
17. Y. F. Wei, C. R. Xie, X. Qing, Y. H. Xu, Control of a new financial risk contagion dynamic model based on finite-time disturbance, *Entropy*, **26** (2024), 999. https://doi.org/10.3390/e26120999
18. S. R. Yan, A. Mohammadzadeh, E. Ghaderpour, Type-3 fuzzy logic and Lyapunov approach for dynamic modeling and analysis of financial markets, *Heliyon*, **10** (2024), e33730. https://doi.org/10.1016/j.heliyon.2024.e33730
19. M. D. Johansyah, S. Vaidyanathan, K. Benkouider, A. Sambas, K. M. Rao, K. Anjaneyulu, Exploring chaos and stability in a 3-D finance model with absolute function nonlinearity, *Mathematics*, **13** (2025), 735. https://doi.org/10.3390/ math13050735

20. A. Phukan, H. K. Sarmah, Bifurcation analysis of a non linear 6D financial system with three time delay feedback, *Chaos Solitons Fractals*, **194** (2025), 116248. https://doi.org/10.1016/j.chaos.2025.116248

21. C. G. Xu, C. Aouiti, M. X. Liao, P. L. Li, Z. X. Liu, Chaos control strategy for a fractional-order financial model, *Adv. Differ. Equations*, **2020** (2020), 573. https://doi.org/10.1186/s13662-020-02999-x

22. Z. Yao, K. H. Sun, S. He, Dynamics of fractional-order chaotic rocard relaxation econometric system, *Int. J. Bifurcation Chaos*, **32** (2022),2250195. https://doi.org/10.1142/S0218127422501954

23. T. Cui, P. J. Liu, Computational modeling of financial sistem via a new fractal-fractional mathematical model, *Fractals*, **31** (2023), 2340083. https://doi.org/10.1142/S0218348X23400832

24. Q. N. Li, R. H. Li, D. M. Huang, Dynamic analysis of a new 4D fractional-order financial system and its finite-time fractional integral sliding mode control based on RBF neural network, *Chaos Solitons Fractals*, **177** (2023), 114156. https://doi.org/10.1016/j.chaos.2023.114156

25. L. Diabi, A. Ouannas, A. Hioual, S. Momani, A. Abbes, On fractional discrete financial system: Bifurcation, chaos, and control, *Chin. Phys. B*, **33** (2024), 100201. https://doi.org/10.1088/1674-1056/ad5d96

26. Z. Xu, K. H. Sun, H. H. Wang, Dynamics and function projection synchronization for the fractional-order financial risk system, *Chaos Solitons Fractals*, **188** (2024), 115599. https://doi.org/10.1016/j.chaos.2024.115599

27. L. M. Pecora, T. L. Carroll, Synchronization in chaotic systems, *Chaos Solitons Fractals*, **64** (1990), 821–824. https://doi.org/10.1103/PhysRevLett.64.821

28. H. Fu, Y. G. Gao, Synchronization of uncertain general fractional unified chaotic systems via finite-time adaptive sliding mode control, *Chaos*, **33** (2023), 043136. https://doi.org/10.1063/5.0130366

29. H. Q. Wang, G. Chai, S. J. Kang, Adaptive fixed-time anti-synchronization and synchronization control for Liu-Chen-Liu chaotic systems with actuator faults, *Int. J. Adapt. Control Signal Process.*, **38** (2024), 2158–2177. https://doi.org/10.1002/acs.3799

30. L. P. Chen, M. Xue, A. M. Lopes, R. C. Wu, X. H. Zhang, Y. Q. Chen, New synchronization criterion of incommensurate fractional-order chaotic systems, *IEEE Trans. Circuits Syst. II Express Briefs*, **71** (2024), 455–459. https://doi.org/10.1109/TCSII.2023.3297174

31. Y. L. Wang, H. Jahanshahi, S. Bekiros, F. Bezzina, Y. M. Chu, A. A. Aly, Deep recurrent neural networks with finite-time terminal sliding mode control for a chaotic fractional-order financial system with market confidence, *Chaos Solitons Fractals*, **146** (2021), 110881. https://doi.org/10.1016/j.chaos.2021.110881

32. S. H. Yuningsih, E. Rusyaman, S. Vaidyanathan, A. Sambas, Investigation of chaos behavior and integral sliding mode control on financial risk model, *AIMS Math.*, **7** (2022), 18377–18392. https://doi.org/10.3934/math.20221012

33. M. D. Johansyah, A. Sambas, S. Mobayen, B. Vaseghi, S. F. Al-Azzawi, Sukono, et al., Dynamical analysis and adaptive finite-time sliding mode control approach of the financial fractional-order chaotic system, *Mathematics*, **11** (2023), 100. https://doi.org/10.3390/math11010100

34. X. M. Zhang, Q. L. Han, J. Wang, Admissible delay upper bounds for global asymptotic stability of neural networks with time-varying delays, *IEEE Trans. Neural Networks Learn. Syst.*, **29** (2018), 5319–5329. https://doi.org/10.1109/TNNLS.2018.2797279

35. L. M. Wang, T. D. Dong, M. F. Ge, Finite-time synchronization of memristor chaotic systems and its application in image encryption, *Appl. Math. Comput.*, **347** (2019), 293–305. https://doi.org/10.1016/j.amc.2018.11.017

36. Y. C. Ding, H. Liu, A new fixed-time stability criterion for fractional-order systems, *AIMS Math.*, **7** (2022), 6173–6181. https://doi.org/10.3934/math.2022343

37. J. D. Sánchez-Torres, D. G. Gómez-Gutiérrez, E. López, A. G. Loukianov, A class of predefined-time stable dynamical systems, *IMA J. Math. Control Inf.*, **35** (2018), i1–i29. https://doi.org/10.1093/imamci/dnx004

38. C. A. Anguiano-Gijón, A. J. Muñoz-Vázquez, J. D. Sánchez-Torres, G. Romero-Galván, F. Martínez-Reyes, On predefined-time synchronisation of chaotic systems, *Chaos Solitons Fractals*, **122** (2019), 172–178. https://doi.org/10.1016/j.chaos.2019.03.015

39. M. J. Zhang, H. Y. Zang, L. Y. Bai, A new predefined-Time sliding mode control scheme for synchronizing chaotic systems, *Chaos Solitons Fractals*, **164** (2022), 112745. https://doi.org/10.1016/j.chaos.2022.112745

40. H. B. Xue, X. H. Liu, A novel fast terminal sliding mode with predefined-time synchronization, *Chaos Solitons Fractals*, **175** (2023), 114049. https://doi.org/10.1016/j.chaos.2023.114049

41. W. Zheng, S. C. Qu, Q. Tang, X. N. Du, Predefined-time sliding mode control for synchronization of uncertain hyperchaotic system and application, *J. Vib. Control*, **31** (2025), 528–538. https://doi.org/10.1177/10775463241228649

42. S. Sahoo, R. Nathasarma, B. K. Roy, Time-synchronized predefined-time synchronization between two non-identical chaotic systems, *Chaos Solitons Fractals*, **181** (2024), 114662. https://doi.org/10.1016/j.chaos.2024.114662

43. C. Jia, X. H. Liu, X. Y. Li, J. Y. Xu, A new adaptive predefined time sliding mode control for nonlinear systems, *IEEE Trans. Circuits Syst. II Express Briefs*, **71** (2024), 2094–2098. https://doi.org/10.1109/TCSII.2023.3332089

44. M. Y. Wang, J. P. Li, Interpretable predictions of chaotic dynamical systems using dynamical system deep learning, *Sci. Rep.*, **14** (2024), 3143. https://doi.org/10.1038/s41598-024-53169-y

45. H. Jahanshahi, Z. H. Zhu, Review of machine learning in robotic grasping control in space application, *Acta Astronaut.*, **220** (2024), 37–61. https://doi.org/10.1016/j.actaastro.2024.04.012

46. R. Zahedifar, M. S. Baghshah, A. Taheri, LLM-controller: Dynamic robot control adaptation using large language models, *Rob. Auton. Syst.*, **186** (2025), 104913. https://doi.org/10.1016/j.robot.2024.104913

47. J. L. Chen, X. S. Zhao, J. Y. Xiao, Novel predefined-time control for fractional-order systems and its application to chaotic synchronization, *Math. Methods Appl. Sci.*, **47** (2024), 5427–5440. https://doi.org/10.1002/mma.9871

48. M. Yang, Q. Zhang, K. Xu, M. Chen, Adaptive differentiator-based predefined-time control for nonlinear systems subject to pure-feedback form and unknown disturbance, *Complexity*, **2021** (2021), 7029058. https://doi.org/10.1155/2021/7029058

49. H. Liu, H. Y. Tu, S. Huang, X. J. Zheng, Adaptive predefined-time sliding mode control for QUADROTOR formation with obstacle and inter-quadrotor avoidance, *Sensors*, **23** (2023), 2392. https://doi.org/10.3390/s23052392

50. Y. Zhang, F. W. Meng, Y. Z. Tai, Neural network-based Predefined-time attitude control for rigid spacecraft with uncertainties and disturbances, *J. Ind. Manage. Optim.*, **21** (2025), 1832–1845. https://doi.org/10.3934/jimo.2024151

51. E. Ahmed, A. M. A. El-Sayed, H. A. A. El-Saka, Equilibrium points, stability and numerical solutions of fractional-order predator–prey and rabies models, *J. Math. Anal. Appl.*, **325** (2007), 542–553. https://doi.org/10.1016/j.jmaa.2006.01.087

52. C. P, Li, W. H. Deng, Remarks on fractional derivatives, *Appl. Math. Comput.*, **187** (2007), 777–784. https://doi.org/10.1016/j.amc.2006.08.163

53. K. Diethelm, *The Analysis of Fractional Differential Equations*, Springer, 2010. https://doi.org/10.1007/978-3-642-14574-2

54. N. X. Liu, J. T. Fei, Adaptive fractional sliding mode control of active power filter based on dual RBF neural networks, *IEEE Access*, **5** (2017), 27590–27598. https://doi.org/10.1109/access.2017.2774264

55. K. Diethelm, N. J. Ford, A. D. Freed, A predictor-corrector approach for the numerical solution of fractional differential equations, *Nonlinear Dyn.*, **29** (2002), 3–22. https://link.springer.com/article/10.1023/A:1016592219341

56. G. C. Wu, Z. G. Deng, D. Baleanu, D. Q. Zeng, New variable-order fractional chaotic systems for fast image encryption, *Chaos*, **29** (2019), 083103. https://doi.org/10.1063/1.5096645

57. L. L. Liu, Q. Zhang, X. P. Wei, A RGB image encryption algorithm based on DNA encoding and chaos map, *Comput. Electr. Eng.*, **38** (2012), 1240–1248. https://doi.org/10.1016/j.compeleceng.2012.02.007

58. Y. W. Yang, J. Gao, H. Imani, Design, analysis, circuit implementation, and synchronization of a new chaotic system with application to information encryption, *AIP Adv.*, **13** (2023), 075116. https://doi.org/10.1063/5.0161382



AIMS Press